Article

Cell Reports

Physiological Tolerance to ssDNA Enables Strand Uncoupling during DNA Replication

Graphical Abstract

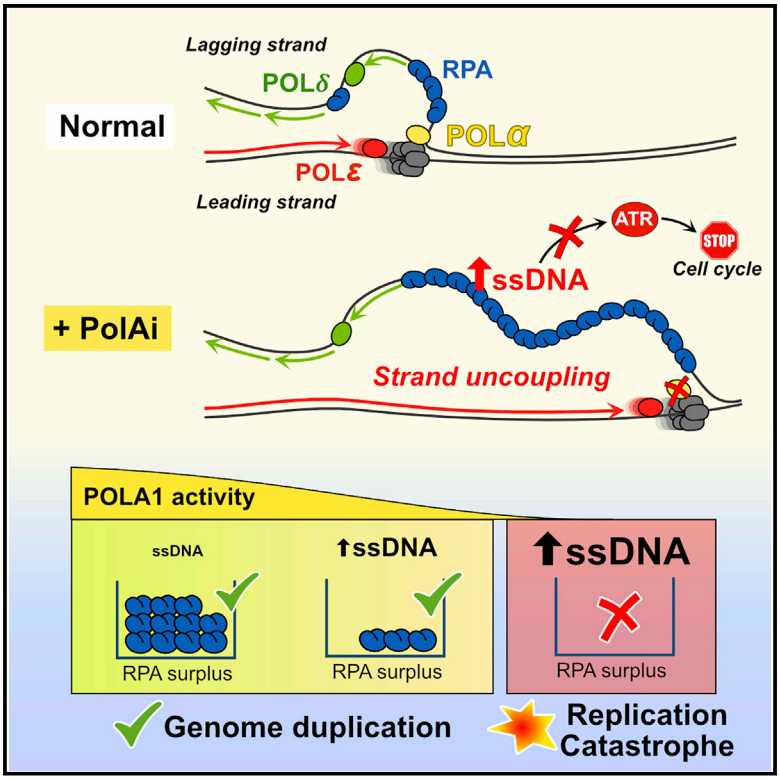

Authors

Amaia Ercilla, Jan Benada, Sampath Amitash, ..., Vincenzo Costanzo, Jiri Lukas, Luis Toledo

Correspondence

ltoledo@sund.ku.dk

In Brief

Using specific POLA1 inhibitors, Ercilla et al. show that DNA synthesis works independently at leading and lagging strands and can be "uncoupled" *in vivo*. The authors show that cells can naturally tolerate ssDNA formation during DNA replication as long as it is protected by the surplus of RPA molecules.

Highlights

- POLA1 inhibitors (PolAis) cause the uncoupling of leading and lagging strand synthesis
- PolAi results in ssDNA formation at the lagging strand and a replication catastrophe
- ssDNA caused by PolAis does not activate an ATR-dependent stress response
- RPA surplus allows cells to duplicate their genome with elevated strand uncoupling and ssDNA

Ercilla et al., 2020, Cell Reports *30*, 2416–2429
February 18, 2020
https://doi.org/10.1016/j.celrep.2020.01.067

CellPress

OPEN ACCESS
CellPress

Cell Reports
Article

Physiological Tolerance to ssDNA Enables Strand Uncoupling during DNA Replication

Amaia Ercilla,[1,4] Jan Benada,[1,5] Sampath Amitash,[1] Gijs Zonderland,[1] Giorgio Baldi,[2] Kumar Somyajit,[3] Fena Ochs,[3,6] Vincenzo Costanzo,[2] Jiri Lukas,[3] and Luis Toledo[1,7,*]

[1]Center for Chromosome Stability, Institute for Cellular and Molecular Medicine, Faculty of Health and Medical Sciences, University of Copenhagen, Copenhagen 2200, Denmark
[2]DNA Metabolism Laboratory, FIRC Institute for Molecular Oncology (IFOM), Milan 20139, Italy
[3]Protein Signaling Program, Novo Nordisk Foundation Center for Protein Research, Faculty of Health and Medical Sciences, University of Copenhagen, Copenhagen 2200, Denmark
[4]Present address: CIC bioGUNE, Bizkaia Technology Park, Derio, Bizkaia 48160, Spain
[5]Present address: Biotech Research & Innovation Centre, Faculty of Health and Medical Sciences, University of Copenhagen, Copenhagen 2200, Denmark
[6]Present address: Department of Biochemistry, University of Oxford, South Parks Road, Oxford OX1 3QU, UK
[7]Lead Contact
*Correspondence: ltoledo@sund.ku.dk
https://doi.org/10.1016/j.celrep.2020.01.067

SUMMARY

It has been long assumed that normally leading strand synthesis must proceed coordinated with the lagging strand to prevent strand uncoupling and the pathological accumulation of single-stranded DNA (ssDNA) in the cell, a dogma recently challenged by *in vitro* studies in prokaryotes. Here, we report that human DNA polymerases can function independently at each strand *in vivo* and that the resulting strand uncoupling is supported physiologically by a cellular tolerance to ssDNA. Active forks rapidly accumulate ssDNA at the lagging strand when POLA1 is inhibited without triggering a stress response, despite ssDNA formation being considered a hallmark of replication stress. Acute POLA1 inhibition causes a lethal RPA exhaustion, but cells can duplicate their DNA with limited POLA1 activity and exacerbated strand uncoupling as long as RPA molecules suffice to protect the elevated ssDNA. Although robust, this uncoupled mode of DNA replication is also an in-built weakness that can be targeted for cancer treatment.

INTRODUCTION

Replication forks need to carry out DNA synthesis by using a distinct mechanism at each strand. In contrast to the leading strand replication, which consists of a simple continuous 5′ to 3′ DNA polymerization by DNA polymerase epsilon (Polε) (O'Donnell et al., 2013), lagging strand synthesis occurs backward in short "Okazaki fragments" (OFs), which require a repetitive time-consuming sequence of events (Okazaki, 1967). For this reason, one could argue that leading and lagging strand machineries are mutually coordinated to progress with the same kinetics at the fork and prevent their uncoupling, which would cause the buildup of potentially harmful levels of single-stranded DNA (ssDNA). ssDNA accumulation is considered a pathological hallmark of replication stress (RS) that can threaten genomic stability, and as such, it is detected by ataxia telangiectasia and Rad3-related (ATR) to trigger the RS response or checkpoint and arrest cell proliferation (Byun et al., 2005; Zou and Elledge, 2003). This can be orders of magnitude higher than the so-called intrinsic or basal ATR checkpoint (Saldivar et al., 2018). Paradoxically, ssDNA accumulates naturally at the lagging strand as the first necessary step for OF generation. How a stress response is not persistently triggered during DNA replication is unclear (Cimprich and Cortez, 2008), but one could argue that ssDNA turns hazardous and activates ATR only beyond a certain threshold that is achieved by RS. Consequently, coordination between leading and lagging strand synthesis would be critical to maintain ssDNA levels low in the nucleus. An extra hazard makes regulating ssDNA homeostasis particularly critical in mammals. ssDNA is a replication intermediate highly vulnerable to nucleolytic attacks that needs to be protected by the binding to Replication Protein A (RPA), as cells suffer a massive and lethal breakage of ssDNA (replication catastrophe [RC]) when their pool of protective RPA molecules is exhausted (Toledo et al., 2013). Although such a scenario is unlikely in physiological conditions because cells have a great excess of RPA protein, the sheer existence of this excess also argues that it has been favored by evolution to respond to hitherto elusive replication-coupled mechanisms that can generate hazardous levels of ssDNA in physiological conditions.

In vitro analyses of DNA replication have proposed a basis for a coordination between leading and lagging strand synthesis (Lee et al., 2006; Stano et al., 2005; Yao et al., 2009), whereas others have hinted that both machineries can work independently to a certain extent in conditions of stress or

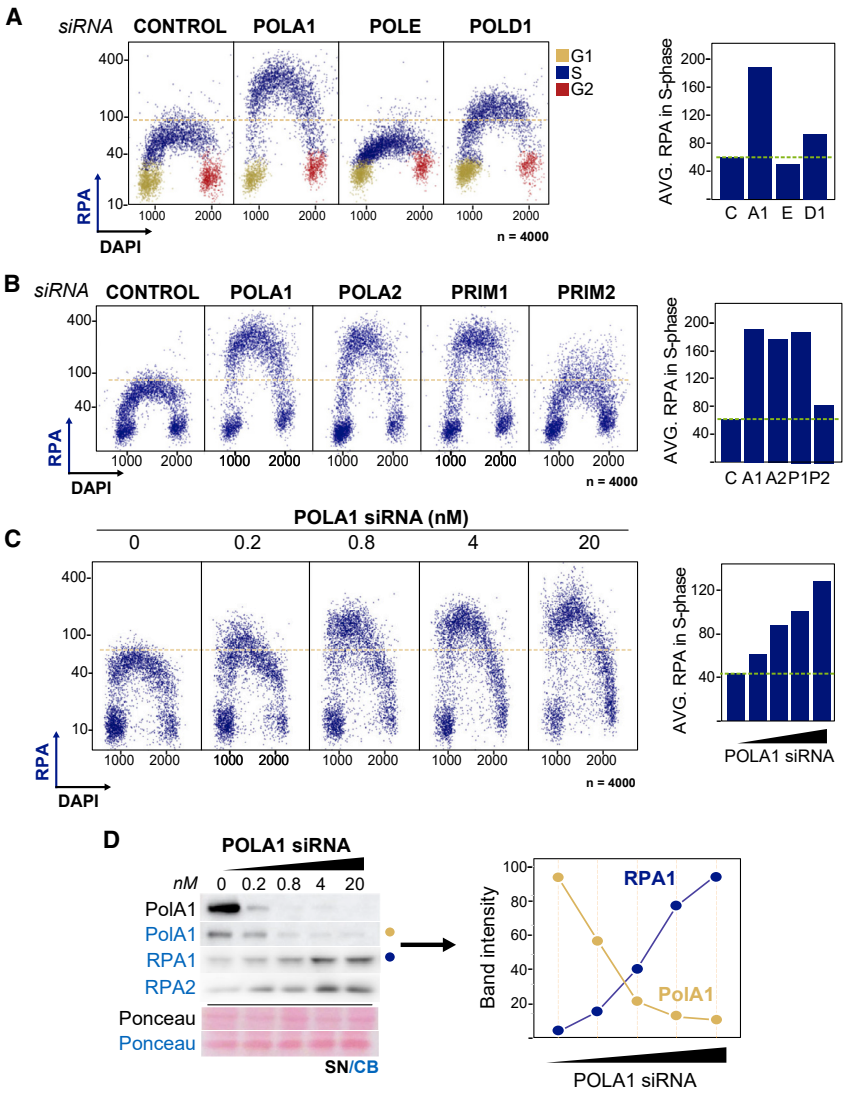

Figure 1. Depletion of POLA1 Causes ssDNA Accumulation Spontaneously in S-Phase

(A) QIBC of chromatin-bound-RPA (CB-RPA)/DAPI of cells transfected with the indicated siRNA (left panel). Bar graph shows average (AVG) CB-RPA values of S-phase cells (identified by EdU incorporation, see Figure S1B) (right panel).

(B) Cells were transfected and stained for CB-RPA and DAPI (left panel). Bar graph shows average CB-RPA values of S-phase cells (right panel).

(C) QIBC of cells transfected with increasing concentrations of POLA1 siRNA and stained for CB-RPA and DAPI (left panel). Bar graph shows the average CB-RPA values of S-phase cells (right panel).

(D) Cells were transfected with increasing concentrations of POLA1 siRNA and processed for western blot (WB; left panel). Quantification of RPA1 and POLA1 levels on chromatin from the blots (right panel). CB, chromatin bound; SN, supernatant.

DNA damage (Gan et al., 2017; Pagès and Fuchs, 2003; Taylor and Yeeles, 2018). However, a more recent analysis of *Escherichia coli* (*E. coli*) DNA replication showed that such coordination is absent, and polymerases act fully independently, concluding that transient events of uncoupling are part of the normal functioning of forks (Graham et al., 2017). This "independent and stochastic" behavior of polymerases could offer a simple and elegant solution to solve the problem of bidirectional replication, but there is no such evidence yet *in vivo*. Such a scenario could favor the stochastic accumulation of ssDNA at replication forks, and thus, how cells would tolerate it in a context of checkpoint surveillance and ssDNA instability remains an outstanding question (Zeman and Cimprich, 2014).

Here, we show that DNA polymerases function independently in living mammalian cells. Using quantitative image-based cytometry (QIBC) (Toledo et al., 2013), we show that a deficient POLA1 activity provokes a vast accumulation of ssDNA *in vivo*, resulting from the uncoupling of leading and lagging strand synthesis (henceforth referred to as "strand uncoupling"). Severe inhibition of POLA1 can exhaust the cell RPA reservoir and cause an RC in only a few minutes, revealing the mode of action and potential clinical applications of the newly identified POLA1 inhibitors. To our surprise, uncoupled forks do not activate a stress response to halt cell cycle progression despite the ssDNA accumulation. Strikingly, cells can sustain persistent levels of strand uncoupling and the ensuing ssDNA accumulation (as long as RPA remains in surplus) without compromising cell proliferation or inducing deleterious RS. Collectively, our work reveals that the independent behavior of leading and lagging strand synthesis is an intrinsic feature of mammalian replisomes supported by an *in vivo* tolerance to ssDNA and an in-built weakness that could be exploited in the treatment of cancer.

RESULTS

Limited POLA1 Activity Causes ssDNA in S-Phase

The immediate consequence of an uncoupling of leading and lagging strand synthesis is the accumulation of ssDNA at active forks. To reveal whether this can happen *in vivo*, we depleted POLA1 (the DNA primase subunit of the POLA complex) with small interfering RNA (siRNA) in U2OS cells, and used QIBC to measure the accumulation of ssDNA by quantifying the levels of chromatin-bound RPA (CB-RPA) in single cells (Toledo et al., 2013). POLA1 depletion caused a clear increase in CB-RPA in S-phase cells (Figure 1A; Figures S1A and S1B). A significant but lower increase was achieved by depleting POLD1, whereas a decrease in CB-RPA was observed after depletion of POLE1. The fact that CB-RPA was specific for lagging strand polymerases (especially of POLA1) and that cells

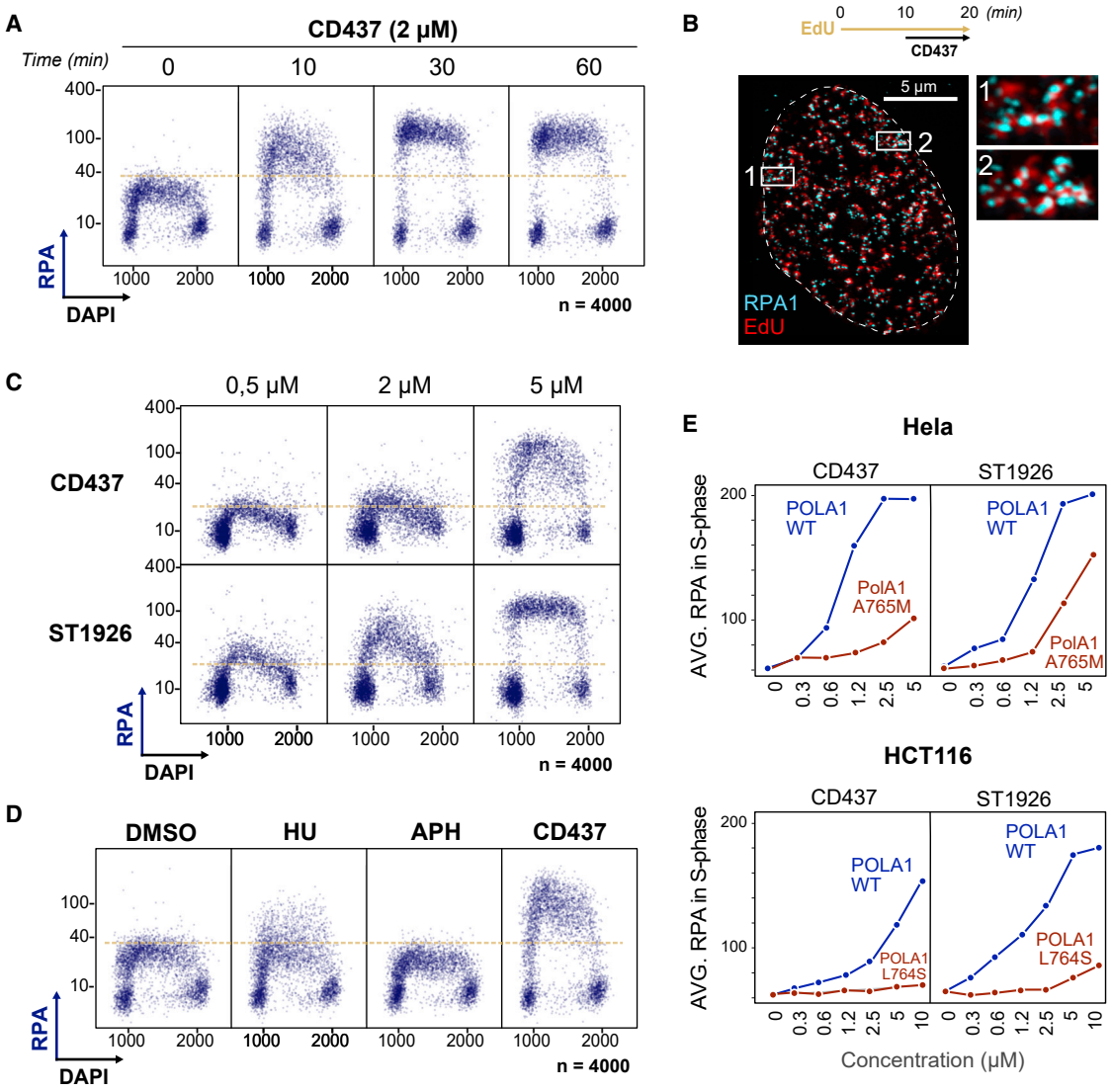

Figure 2. POLA1 Inhibitors Trigger a Fast Accumulation of ssDNA in Replicating Cells

(A) Cells were treated with CD437, stained for CB-RPA/DAPI, and analyzed by QIBC.

(B) Representative image of cells labeled with EdU, treated with 10 μM CD437, and stained for CB-RPA1 and EdU. Colocalization of CB-RPA1 and EdU signals is shown.

(C) QIBC of cells treated for 10 min with CD437 or ST1926 and stained for CB-RPA/DAPI.

(D) QIBC of cells treated with DMSO, 2 mM HU, 4 μM APH, or 1 μM CD437 and stained for CB-RPA/DAPI.

(E) PolA1 wild-type (WT) and mutant (residue is indicated) HeLa and HCT116 cells were treated for 1 h with increasing CD437 or ST1926 concentrations, stained for CB-RPA/DAPI, and analyzed by QIBC. Average CB-RPA levels are shown.

were actively replicating (Figure S1B) indicate that such a spontaneous accumulation of ssDNA could be explained by a strand uncoupling, as it has been observed for *E. coli* DNA replication *in vitro* (Graham et al., 2017). Notably, the depletion by siRNA of any of the other members of the POLA complex resulted in a destabilization of POLA1 and an accumulation of CB-RPA (Figures 1B and S1C). Collectively, these results indicate that the integrity of the POLA complex is critical to prevent strand uncoupling and suggest that POLA1 is the rate-limiting component. In fact, the extent of uncoupling was inversely proportional to the levels of POLA1 on chromatin, as revealed by the increase in CB-RPA when POLA1 was gradually depleted in U2OS cells (Figures 1C and 1D). To investigate this further and to avoid the limitations of siRNA depletion, we sought to validate the newly identified POLA1 inhibitors as tools to study strand uncoupling *in vivo*.

A recent study identified the adamantyl retinoid CD437 as a direct allosteric inhibitor of POLA1 (Han et al., 2016). To test whether CD437 can mimic the effect of POLA1 depletion, we first exposed U2OS cells to CD437 and measured CB-RPA as before. CB-RPA levels in S-phase swiftly increased after adding CD437 to the medium (Figure 2A), suggesting a sudden strand

uncoupling at active replication forks. Supporting this, RPA accumulated in areas of 5-ethynyl-2'-deoxyuridine (EdU) incorporation (Figure 2B). A number of retinoids similar to CD437 have been generated (Pérez-Rodríguez et al., 2009), and those with a CD437-like structure also induced CB-RPA in U2OS cells (Figure S2A). This included ST1926, which has also been shown to inhibit POLA1 *in vitro* and was even more potent than CD437 in inducing CB-RPA (Figure 2C; Abdel-Samad et al., 2018). In comparison to CD437, other commonly used inhibitors of DNA synthesis, such as hydroxyurea (HU) or aphidicolin (APH) that prevent the activity of all replicative polymerases (Figure S2B), caused only a mild or undetectable increase in CB-RPA (Figure 2D). To confirm that POLA1 inhibition was responsible for the appearance of ssDNA, we analyzed the response to ST1926 and CD437 in CD437-resistant cells (Han et al., 2016). These cells express a mutated POLA1 that conserves its enzymatic activity but is resistant to CD437 *in vitro*. We used a previously published HCT116 clone carrying a L764S mutation (introduced by CRISPR) and a HeLa clone where we identified a novel mutation (A765M) by sequencing the POLA1 gene (Figure S2C). Both cell lines failed to accumulate CB-RPA at concentrations of CD437 or ST1926 that suffice to cause massive ssDNA in their wild-type counterparts (Figures 2E and S2D). These results confirm that the increase in CB-RPA caused by CD437/ST1926 is triggered by specifically inhibiting POLA1, mimicking the depletion of the protein *in vivo*. These data also suggest that the mechanism of action differs from that elicited by inhibitors of DNA replication, so we next sought to investigate whether this could be strand uncoupling. We chose ST1926 to continue our study as it was the most potent of all tested retinoids (Figure S2A). No major additional speed in ssDNA generation was observed beyond a concentration of 10 μM (Figure S2E), so we chose this as the highest in our assays. For simplicity, we henceforth refer to ST1926 as POLA1 inhibitor (PolAi).

Inhibition of POLA1 Causes Strand Uncoupling

The reason why POLA1 inhibition causes a strand uncoupling is that the replicative helicases (in eukaryotes, the Cdc45-MCM-GINS complex [CMG]) can still move forward together with the leading strand polymerase despite that DNA synthesis is abrogated at the lagging strand (see model in Figure 7A). Experimentally, such a scenario should fulfill a number of criteria. The first one is that the accumulation of ssDNA should be determined by the speed of DNA unwinding at the fork. As forks normally progress 1–2 kilobases per minute (Jackson and Pombo, 1998), ssDNA should appear extraordinarily fast when POLA1 is inactive. ssDNA can be generated at replication forks by other mechanisms, for instance by causing an uncoupling of the replicative helicase at the fork when all polymerases are stalled. This can be induced by APH or HU, and although it can lead to very long ssDNA stretches at the fork in a *Xenopus laevis* reconstituted system (Walter and Newport, 2000), recent data suggest that it is much more restrained *in vivo* (Zellweger et al., 2015). As expected, PolAi induced ssDNA orders of magnitude faster than APH or HU (Figure 3A). Such speed could not be matched even when HU was combined with inhibitors of ATR or CHK1, which was the fastest way we knew of to induce ssDNA in a human cell (Toledo et al., 2013; Figures 3A and 3B; Videos S1, S2, and S3). Remarkably, RPA foci were clearly visible as early as 5 min after addition of PolAi (Figure 3B). To further support that the CMG is responsible for the appearance of ssDNA, we reasoned that slowing down the CMG by inhibiting the leading strand polymerase should counteract the generation CB-RPA (Graham et al., 2017; Sparks et al., 2019; Taylor and Yeeles, 2019). Indeed, the addition of APH prevented DNA synthesis and strand uncoupling in a dose-dependent manner (Figures 3C and S3A). Accordingly, depletion of Timeless, which has been recently shown to reduce specifically the motion of replication forks (Somyajit et al., 2017), also led to a reduction of speed in ssDNA generation after PolAi (Figure S3B). The second criterion for a scenario of strand uncoupling is that, as the parental DNA is unwound, ssDNA should accumulate in the form of long stretches in one of the strands. To explore this, we first monitored the morphology of CB-RPA in human cells by structured illumination microscopy (SIM). Remarkably, PolAi led to a variety of asymmetrically shaped and large RPA structures, which contrasted with the smaller and round foci caused by HU (Figures 3D and S3C). In addition, we used an established technique to visualize ssDNA accumulation in fork structures in *Xenopus laevis* egg extracts by electron microscopy (EM). As in human cells, PolAi induced CB-RPA in sperm DNA (Figure S3D), and in all conditions (including untreated nuclei), the majority of forks showed single ssDNA gaps adjacent to the fork junction in one of the strands (Figures 3E and 3F). Remarkably, the length of those gaps was increased in a PolAi-dependent manner (Figures 3E and 3F), in some cases up to 2 Kb. Occasionally, we also detected single lagging gaps, which were particularly long at the highest PolAi concentration (100 μM, 120 min), or several smaller ones, suggesting the accumulation of unfinished OFs at the lagging strand (Figure S3E). The last criterion is that ssDNA accumulation and DNA synthesis should be happening simultaneously, indicative of the status of each strand. This is, for instance, opposite to a scenario of helicase uncoupling from stalled polymerases, where ssDNA accumulates slowly as a result of fork stalling and only after DNA synthesis plummets (Figure 3G). In sharp contrast, PolAi (1 μM) caused a rapid increase in ssDNA that did not significantly affect overall DNA synthesis (Figure 3G). This was also shown by DNA fiber analysis, as most forks continued after PolAi (1 μM) (Figure S3F) and their progression was unaffected despite the simultaneous buildup of ssDNA (Figure S3G). By contrast, labeled DNA fibers were shorter at very high PolAi (50 μM), which could be explained by the fact that cells already entered RC after the first 5 to 10 min at high PolAi (Figure S3H). This indicates that leading strand synthesis was temporarily unaffected (before RC) despite POLA1 being fully inhibited. Supporting this, EdU incorporation in the first 5 min was nearly half of the control, potentially accounting for the DNA synthesis still taking place at normal rates on the leading strand of active forks (Figure S3I). Finally, we imaged by SIM cells treated with PolAi and EdU simultaneously to see whether ssDNA accumulation and DNA synthesis would colocalize spatiotemporally. Interestingly, RPA and EdU signals were intertwined, occupying adjacent spaces rather than colocalizing (Figure 3H), potentially indicating a separation in sister chromatids. Collectively, this evidence confirms the notion that POLA1 inhibition leads to a strand uncoupling.

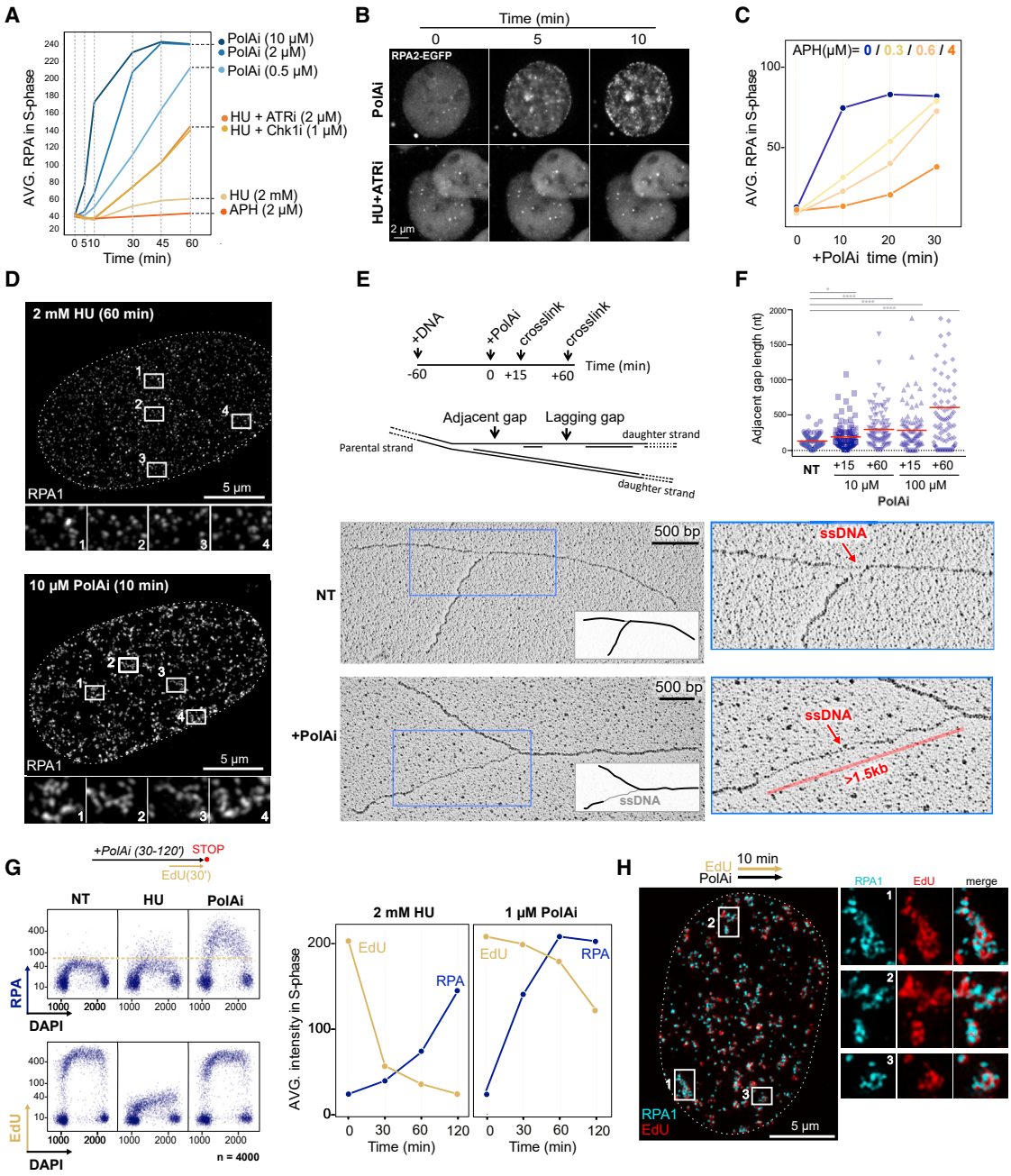

Figure 3. PolAi Trigger ssDNA by Strand Uncoupling

(A) Cells were treated with the indicated drug and stained for CB-RPA. Average CB-RPA intensities are displayed.

(B) Representative images of Video S1 where U2OS/RPA2-EGFP cells were treated with 10 μM PolAi or 2 mM HU + 2 μM ATR.

(C) Cells were pre-incubated with APH for 10 min and then 5 μM PolAi was added to the media. CB-RPA levels were analyzed by QIBC. Average CB-RPA intensities are displayed.

(D) Representative images obtained by SIM. Insets illustrate CB-RPA1 structures.

(E) Schematic of a replication fork presenting the position of gaps scored as adjacent and lagging (top panel). Representative EM micrographs showing adjacent gaps isolated from NT or PolAi-treated (10 μM; 15 min) extracts (bottom panel). ssDNA gaps are indicated. NT, non-treated.

(F) The length of the ssDNA gaps from (E) in each condition (n = 100) are shown. Red lines indicate average values.

(G) Cells were treated with 2 mM HU or 1 μM PolAi for 30 min and analyzed by QIBC. EdU was added during the last 30 min of treatment. Average values for CB-RPA and EdU for the indicated times (right panel).

(H) Representative SIM images of cells treated with EdU and 10 μM PolAi for 10 min and stained for CB-RPA1 and EdU. Insets illustrate how EdU and RPA1 signals are intertwined but not colocalizing.

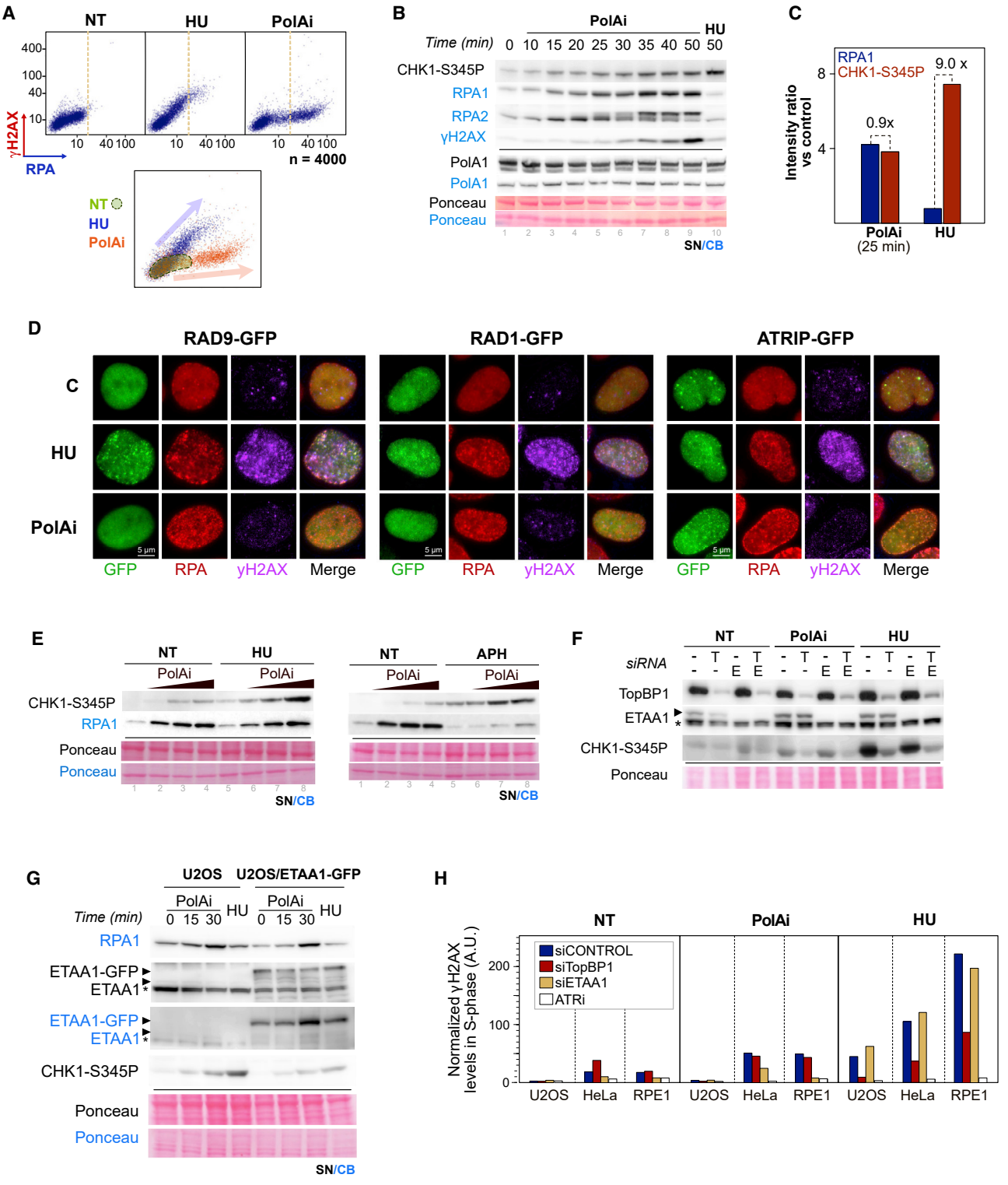

Figure 4. ssDNA Generated by Strand Uncoupling Enhances ATR Signaling but Does Not Trigger a Replication Checkpoint

(A) Cells were treated with 2 mM HU or 1 μM PolAi for 30 min and analyzed by QIBC. QIBC of γH2AX/CB-RPA (top panel). Overlap of the QIBC plots (bottom panel). NT, non-treated.

(B) Cells were treated with 1 μM PolAi or 2 mM HU, and soluble (SN) and chromatin (CB) fractions were isolated and analyzed by WB. PolA1 was used as a loading control.

(legend continued on next page)

ssDNA Does Not Trigger a RS Response

Our data confirm that polymerases behave independently *in vivo*, a mode of action that could promote the accumulation of ssDNA. In a cellular context of fork stalling or DNA damage, the formation of ssDNA is closely associated with the activation of an ATR-dependent stress response (Zeman and Cimprich, 2014). Studies using *Xenopus laevis* egg extracts have shown, however, that ssDNA alone fails to activate ATR (Byun et al., 2005; MacDougall et al., 2007). We, therefore, wondered whether ssDNA accumulation by uncoupling (in the absence of additional stress) is sufficient to trigger a stress response *in vivo*. In fact, a failure to activate ATR could be consistent with the little impact of PolAi on DNA synthesis (Figure 3G) (although checkpoint activity has no major role in EdU incorporation in stressed cells; Figure S4A). To address this directly, we first looked at a specific marker of ATR activation by QIBC, the phosphorylation of H2AX (γH2AX) associated with CB-RPA (Toledo et al., 2013). After HU treatment, CB-RPA and γH2AX levels tightly correlated, whereas PolAi induced almost no γH2AX despite the vast increase in CB-RPA (Figure 4A). To explore this further, we monitored the phosphorylation of CHK1, the main ATR downstream target, which regulates the global stress response to target cyclin dependent kinases, or CDKs (Toledo et al., 2017). Despite the extensive CB-RPA, PolAi only caused a slight gradual increase in CHK1 phosphorylation (CHK1-P) over time (Figure 4B). Surprisingly, HU triggered a strong CHK1-P before any significant RPA loading was detected (Figures 4B and S4B). In fact, when CHK1-P levels in Figure 4B were normalized to CB-RPA, HU was 10 times more potent than PolAi in activating ATR (Figure 4C). We wondered whether these results could be consistent with the behavior of the 9-1-1 complex, which is recruited to stalled forks and is critical for ATR activation via TOPBP1 (Delacroix et al., 2007). Interestingly, both RAD9-GFP and RAD1-GFP accumulated in replication foci (marked by RPA) after RS (HU) but not after PolAi (Figures 4D and S4C; Warmerdam et al., 2010). This accumulation correlated with ATR activation detected by γH2AX. In contrast, ATR interacting protein (ATRIP) clearly colocalized with RPA also in PolAi-treated cells, despite no γH2AX being detected in these cells (Figure 4D). Together, these results suggest two kinetically distinct forms of signaling at the fork. The stalling of DNA polymerases (e.g., by HU) triggers an efficient activation of ATR by recruitment of the 9-1-1 complex, even without additional generation of ssDNA. In contrast, the accumulation of RPA rather works to recruit ATR by ATRIP and to amplify the signaling cascade. In fact, the slow rise in CHK1-P after PolAi in Figure 4B followed a linear correlation with the increase of CB-RPA (Figure S4D), a result also reproduced after depleting POLA1 (Figure S4E). We tested then whether these two distinct mechanisms can cooperate. Indeed, a combined treatment of PolAi with HU or APH, which enhanced the amount of ssDNA in both conditions (compare lanes 2 versus 6 and subsequent), amplified CHK1-P proportionally to the increased levels of CB-RPA (Figure 4E). ATR can be activated in the cell by TOPBP1 and/or ETAA1, and previous studies have shown that CHK1-P is largely ETAA1 independent after RS (Bass et al., 2016; Haahr et al., 2016; Kumagai et al., 2006). Because ETAA1 targets ATR by binding RPA directly, we wondered whether PolAi-induced ssDNA could induce CHK1-P in an ETAA1-dependent manner. However, CHK1-P caused by PolAi (or HU) remained TOPBP1 dependent but ETAA1 independent (Figures 4F and S4F). CHK1-P levels after PolAi were mild even in U2OS cells overexpressing ETAA1-GFP and in other cell lines that naturally express high levels of ETAA1, such as hTERT-RPE1 and HeLa (Haahr et al., 2016; Figures 4G, S4F, and S4G). On the contrary, all three cell lines harboring higher ETAA1 levels displayed an ETAA1-dependent rise in γH2AX after PolAi (Figures 4H, S4H, S4I, and S4J), indicating that ATR can still be activated by ETAA1 at RPA-coated ssDNA and phosphorylate other targets at or near the fork. Interestingly, γH2AX was higher and largely TOPBP1 dependent after HU use (Figure 4H), suggesting that TOPBP1 is still the main ATR activator in response to fork stalling. Together, these results establish that fork stalling, and not ssDNA accumulation, is essential for the activation of a stress response.

POLA1 Activity Prevents a RC

S-phase cells have a basal level of ssDNA that closely correlates with DNA synthesis (Figures 5A and S5A). Although neither the basal nor increased amounts of ssDNA trigger a stress response (Figure 4), growing levels of strand uncoupling may eventually become unsustainable *in vivo* by causing an exhaustion of RPA molecules. Remarkably, the swift increase in CB-RPA caused by PolAi led to an RC in virtually all cells in S-phase (Figures 5B and S5B). This was reproduced in multiple cell lines (Figure S5C). RC has been thought to be associated exclusively with artificial conditions of RS, inactivation of ATR/CHK1 kinases, and the ensuing massive firing of dormant origins (Toledo et al., 2013). However, neither ssDNA generation nor DNA damage (RC) by PolAi required CDK or CDC7 activity, reinforcing the idea that PolAi causes ssDNA by strand uncoupling (Figures 5C and S5D). These results highlight that there is no manifest response that can restrain strand uncoupling even to prevent RC and that, therefore, a high POLA1 activity is key to keep physiological ssDNA levels low and far from

(C) The blots from (B) were used to calculate the fold increase in CB-RPA1 and CHK1-S345P levels (versus control). Numbers indicate the relative fold of CHK1-S345P levels versus CB-RPA1.

(D) RAD9-GFP-, RAD1-GFP-, or ATRIP-GFP-transfected U2OS cells were treated with the indicated drugs (HU: 2 mM, 1 h; PolAi: 1 μM, 25 min). Representative images of cells labeled with RPA or γH2AX are shown. See also Figure S4C. C, control.

(E) Cells were treated with HU (2 mM, left panel) or APH (4 M, right panel) and increasing concentrations of PolAi (0.5, 1, 2 μM) for 30 min. Soluble and chromatin fractions were analyzed by WB.

(F) Cells were transfected with control (−), TOPBP1 (T), or ETAA1 (E) siRNAs and treated with 1 μM PolAi or 2 mM HU for 30 min. Whole cell extracts (WCEs) were analyzed by WB. Asterisk indicates non-specific band.

(G) U2OS cells and U2OS/ETAA1-GFP cells were treated and analyzed as in (B). Asterisk indicates non-specific band.

(H) U2OS, HeLa, and hTERT-RPE1 (RPE1) cells were transfected (or incubated with 2 μM ATRi) and treated with 200 nM PolAi or 2 mM HU for 2 h. Cells were analyzed by QIBC; the bar graph shows the average values for γH2AX (arbitrary units [A.U.]) in S-phase cells normalized to G1.

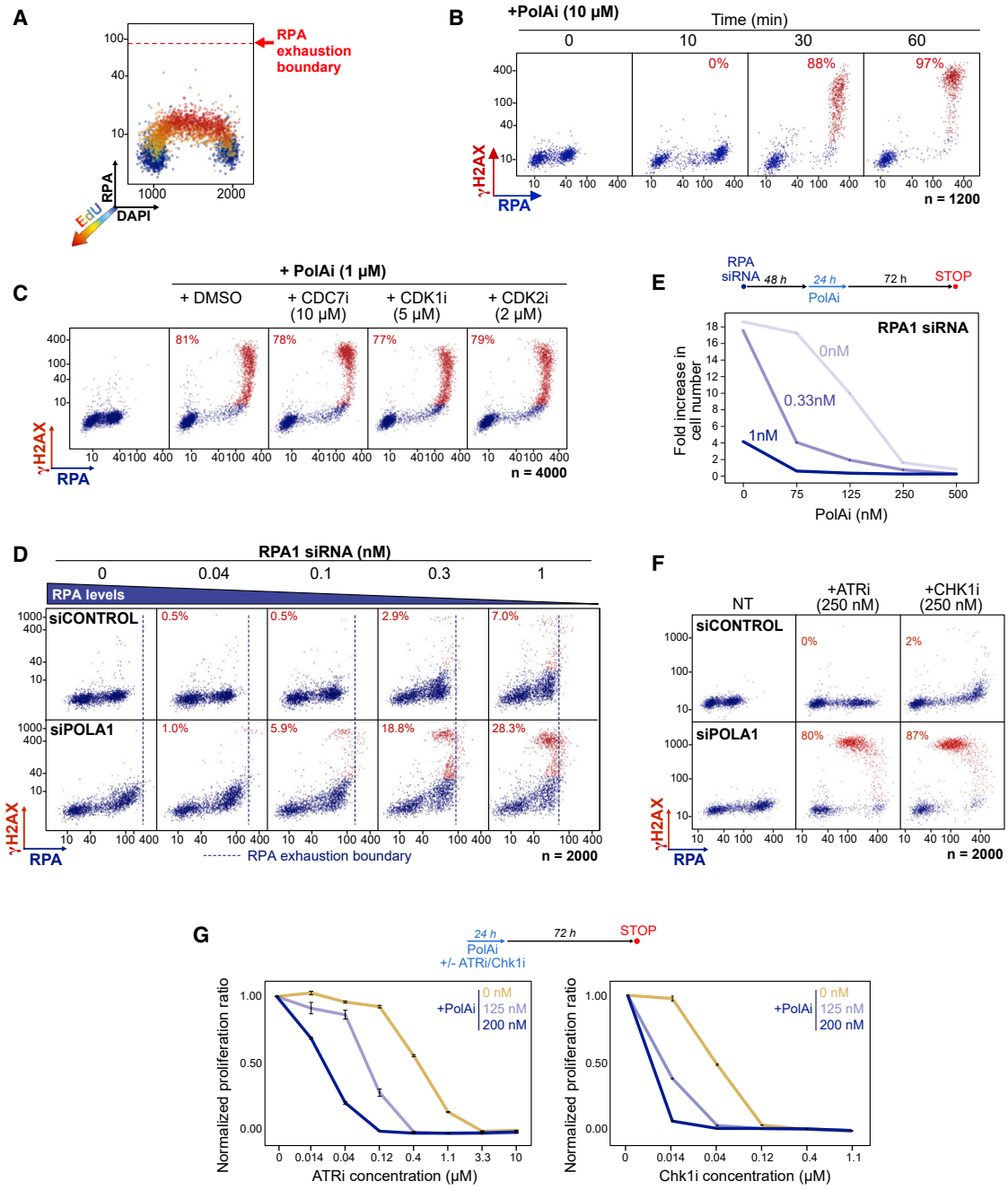

Figure 5. POLA1 Activity Limits Strand Uncoupling and Prevents a Lethal Replication Catastrophe

(A) EdU/RPA/DAPI QIBC showing that RPA levels in S-phase correlate with DNA synthesis. The RPA exhaustion boundary is indicated. See also Figure S5A.

(B) Cells were treated with PolAi, stained for γH2AX/CB-RPA and analyzed by QIBC. The percentage of cells in RC is indicated.

(C) Cells were treated with PolAi ± the indicated drug for 1 h and analyzed by QIBC for γH2AX/CB-RPA. See also Figure S5D.

(D) Cells were transfected with control or POLA1 siRNA + the indicated RPA1 siRNA concentrations and analyzed by QIBC. Dashed lines indicate the relative remaining amount of RPA. The percentage of cells in RC is indicated.

(E) U2OS/H2B-EGFP cells were transfected with RPA1 siRNA and treated as indicated. Lines show the fold change in cell number at 72 h versus time 0 h.

(F) QIBC analysis of cells transfected with control or POLA1 siRNA treated with ATRi or Chk1i for 1 h and stained for γH2AX/CB-RPA. Numbers indicate percentage of cells with RC. NT: non-treated.

(G) U2OS/H2B-EGFP cells were treated with PolAi ± ATRi (left panel) or Chk1i (right panel) for 24 h and released into fresh media for 72 h. Lines show the fold changes in cell number after 72 h (versus time 0 h) normalized to no ATRi or Chk1i. Error bars represent SD.

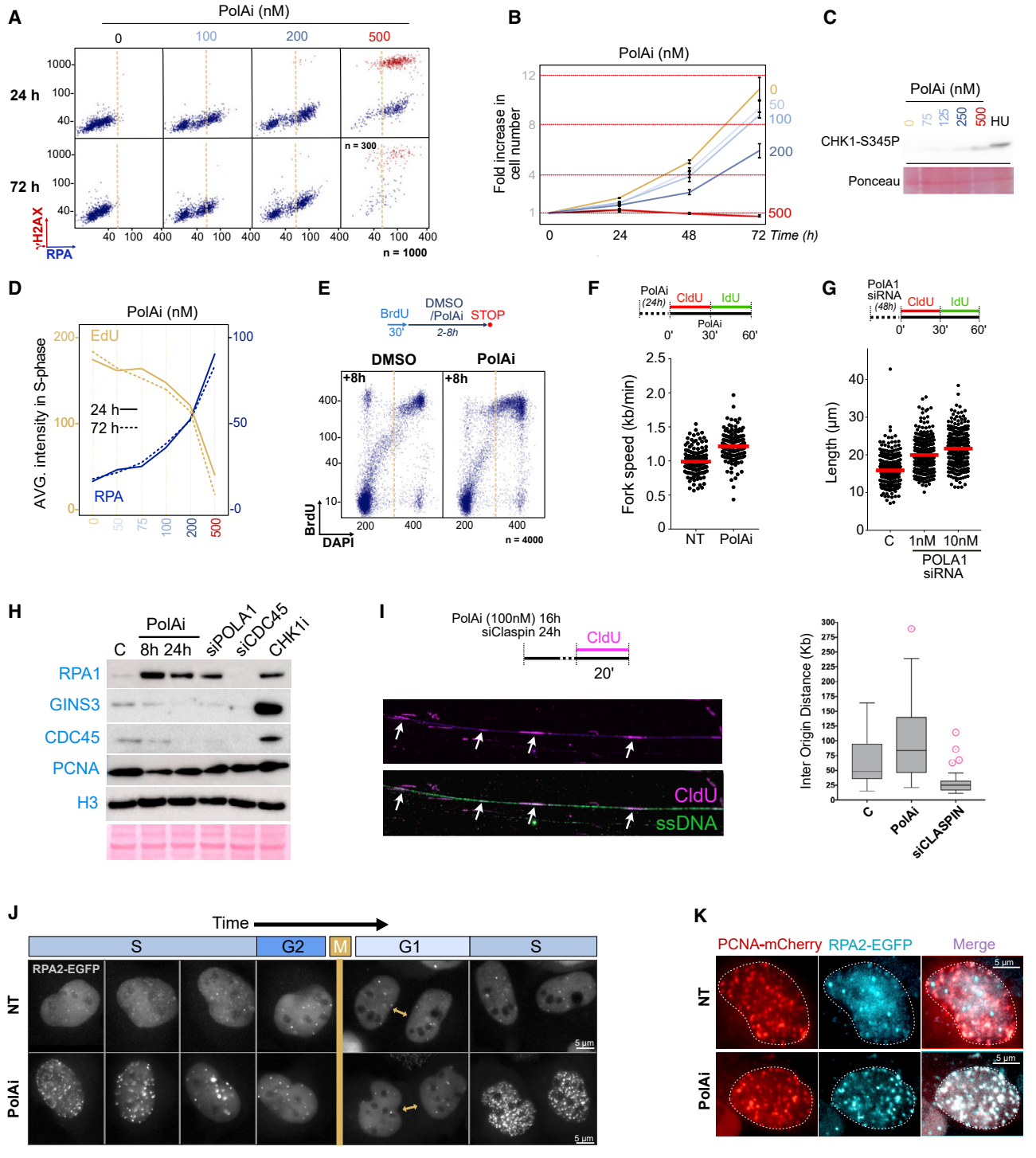

Figure 6. Persistent Levels of Strand Uncoupling Do Not Impede Cell Proliferation

(A) QIBC of γH2AX/CB-RPA of cells treated with PolAi. The cells in RC are highlighted in red. Only 300 cells could be collected at 72 h/500 nM because of the high cell death.

(B) Cells were grown in PolAi and then collected for QIBC. DAPI was used to count the number of cells. Lines show the fold change in cell number versus time 0 h. Error bars represent SD.

(C) WB of cells treated with PolAi or 2 mM HU for 24 h.

(D) Cells were treated as in (A) and labeled with EdU (last 30 min). Lines show average nuclear CB-RPA and EdU levels.

(legend continued on next page)

RPA exhaustion (Figure 1D). Having an excess of RPA is, thus, critical to prevent RC by strand uncoupling and ensure cell survival if POLA1 levels are limiting (Figure 5D, 5E, S5E, and S5F). Consistently, cells with limited POLA1 activity become particularly sensitive to the inhibition of the intrinsic S-phase checkpoint (with ATR or CHK1 inhibitors), which multiplies the demand for RPA by firing new origins (Syljuåsen et al., 2005; Toledo et al., 2013; Figures 5F and S5F). These data indicate that POLA1 activity (by limiting strand uncoupling) and the intrinsic S-phase checkpoint (by constraining the number of active forks) independently cooperate to limit the intrinsic levels of ssDNA and prevent an RC, which explains that PolAi and ATR/CHK1 inhibitors synergize in killing proliferating cells (Figure 5G). This result is particularly interesting for the therapeutic prospect of PolAi/ST1926 (see Discussion).

Cells Can Proliferate with Strand Uncoupling

Because strand uncoupling has a stochastic nature, one could argue that, as a safety mechanism, DNA replication has evolved to function regardless of the degree of ssDNA accumulation at replication forks. Theoretically, a range of different ssDNA levels would be tolerated by the checkpoint and buffered by the surplus of RPA. To address this experimentally, we first tested whether we could create conditions of persistent uncoupling without reaching RPA exhaustion. Indeed, low concentrations (100–200 nM) of PolAi (low-PolAi) lead to a stable increase in CB-RPA without triggering RC (Figure 6A). Remarkably, cells were able to proliferate in low-PolAi, despite the sustained increase in CB-RPA in S-phase throughout the assay (Figures 6A and 6B). Consistently, a transient depletion of POLA1 had little effect on cell proliferation (Figure S6A). The growth arrest observed at higher concentrations of PolAi correlated with widespread RC (Figures 6A and 6B). Confirming the checkpoint tolerance to ssDNA, cells treated with low-PolAi showed no significant CHK1 phosphorylation (Figure 6C). Importantly, these results were recapitulated in hTERT-RPE cells despite the high ETAA1-dependent γH2AX levels (Figures S6B, S6C, and S6D). We obtained a similar result by colony formation, where again cells with a mutated POLA1 showed resistance to PolAi (Figure S6E). Interestingly, the slower cell growth under low-PolAi was due to a reduction in overall DNA synthesis rates (and not by a cell cycle arrest) (Figures 6D, 6E, S6F, and S6G), suggesting that low-PolAi slows down replication forks. However, the average fork progression was increased, despite priming being affected by low-PolAi (Figures 6F, 6G, and S6H). These data together infer that cells under low-PolAi replicate with a reduced number of active forks. In agreement, low-PolAi caused reduced chromatin-bound levels of proteins that are associated specifically with active forks (CDC45, GINS, and PCNA) and an increased inter-origin distance (IOD) (Figures 6H and 6I). This reduced origin firing could be due to the slower priming on the leading strand. As shown by previous studies, low-PolAi likely reproduces a situation where fewer active forks can progress faster due to the higher relative deoxyribonucleotide triphosphate (dNTP) availability (Anglana et al., 2003; Boos et al., 2013).

The fact that cells can complete DNA replication in low-PolAi implies that the enlarged ssDNA structures appearing in S-phase are dynamic and fully resolved before cells enter mitosis. To visualize that, we live-imaged U2OS cells stably expressing RPA2-EGFP in the presence of low-PolAi. Cells showed bigger and brighter RPA foci throughout S-phase, which indeed dissolved before mitosis (Figure 6J; Video S4). We repeated this in cells also expressing mCherry-PCNA, where the timing of RPA foci dissolution closely correlated with PCNA dynamics and its disappearance from replication factories prior to mitosis (Figures 6K and S6I; Video S5). Remarkably, these cells did not carry unresolved replication intermediates that gave rise to mitotic or postmitotic pathologies (Figure S6J), such as the activation of mitotic DNA synthesis (MiDAS), the appearance of ultra-fine bridges (UFBs) in anaphase, or the formation of 53BP1 bodies after cytokinesis (Chan et al., 2009; Lukas et al., 2011; Minocherhomji et al., 2015). Together, these data indicate an exacerbated strand uncoupling does not jeopardize DNA replication, showing that forks can efficiently perform lagging strand synthesis within enlarged or oversized ssDNA loops, provided RPA levels suffice to protect them (Figure 7; Discussion).

DISCUSSION

Pioneering yeast studies have shown evidence of uncoupling in pathological scenarios, particularly how lagging strand synthesis can progress when the leading is stalled (Gan et al., 2017; Pagès and Fuchs, 2003; Taylor and Yeeles, 2018). Our work provides the first evidence that leading strand synthesis can function independently of the lagging strand *in vivo*, recapitulating a recent study that reconstituted *E. coli* DNA replication *in vitro* (Graham et al., 2017). A reduced activity of POLA1 is sufficient to cause a

(E) Cells were labeled for 30 min with BrdU and then released in the presence of 125 nM PolAi or DMSO. After that, cells were stained for BrdU/DAPI and analyzed by QIBC. Yellow dashed line indicates a relative 3-nt DNA content as reference.
(F) DNA fibers of cells treated with 125 nM PolAi for 24 h and labeled with CldU/IdU. Scatterplot showing fork speeds, calculated based on CldU+IdU track length (see STAR Methods for details). Red lines indicate average values. NT, non-treated.
(G) DNA fibers of cells transfected with the indicated siRNA and labeled with CldU/IdU. Scatterplots showing the length of the CldU+IdU tracks. Red lines indicate average values. C, control.
(H) Cells were treated with PolAi (100 nM) or siRNA transfection for the indicated time and collected for WB. WCE were analyzed with the indicated antibodies. C, control.
(I) Cells were transfected with the indicated siRNA and treated as indicated. DNA fibers were prepared, and IOD distances calculated (see STAR Methods for details).
(J) U2OS/RPA2-EGFP cells were grown in 125 nM PolAi and imaged for 24 h (see STAR Methods for details). Representative images of two single cells time-lapse are shown and the relative cell cycle phase. See also Video S4.
(K) U2OS/RPA2-EGFP/PCNA-mCherry cells were assayed as in (J). Representative images of the time-lapse illustrating RPA2 and PCNA colocalization. See also Figure S6I and Video S5.

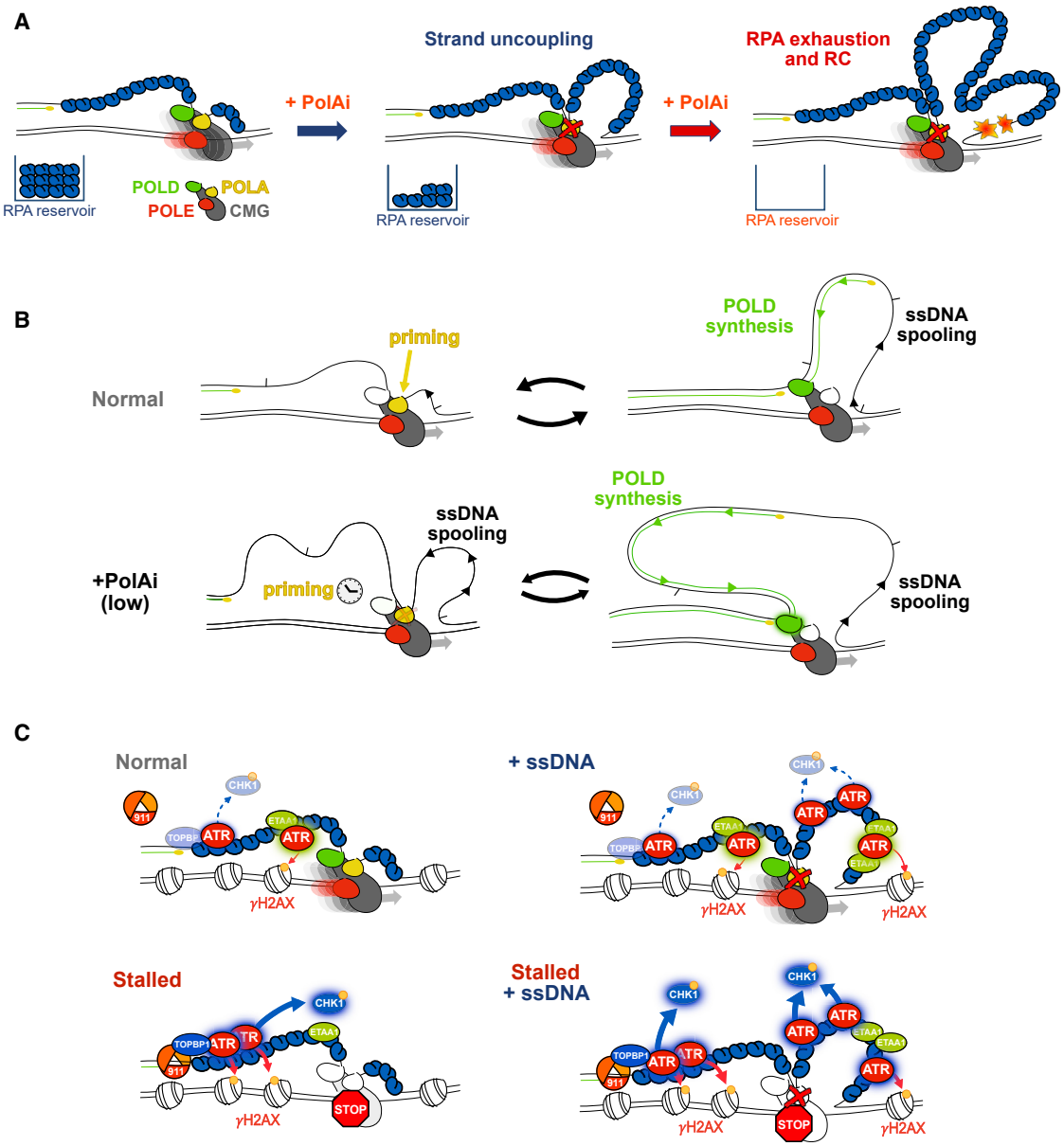

Figure 7. Models

(A) Model for ssDNA accumulation upon PolA1 inhibition. Lagging strand synthesis stalls at the DNA priming step upon POLA1 inhibition, whereas the CMG and POLE keep progressing on the leading strand. Consequently, ssDNA accumulates in front of POLA due to the unwinding of the parental strand. The RPA reservoir can quickly be exhausted, causing the breakage of ssDNA at uncoupled forks.

(B) Model for uncoupled DNA replication. Forks accumulate ssDNA at the lagging strand, and POLA primes and POLD synthesizes the previous Okazaki fragment. This process is repeated cyclically throughout the life of the fork. When POLA1 is partially inhibited, there is an unusual buildup of ssDNA during the priming step, resulting in bigger ssDNA loops at the lagging strand. For this situation to be sustainable, POLD must polymerase much faster than POLE to compensate for the delay in the priming step and keep ssDNA homeostasis, preventing RPA exhaustion.

(C) Model for checkpoint signaling. The accumulation of RPA (top right panel) at an uncoupled fork recruits ETAA1, which stimulates ATR activity toward targets, such as H2AX, but only amplifies the basal checkpoint signaling toward CHK1. Upon fork stalling (bottom left panel), 9-1-1/TOPBP1 efficiently engages and activates ATR without the need of additional RPA. In this scenario, ATR triggers a strong TOPBP1-dependent phosphorylation cascade toward its targets, including CHK1. When extra RPA accumulates in addition to fork stalling (bottom right panel), potentially more ATR molecules can be recruited and activated by TOPBP1, leading to a stronger checkpoint signaling.

spontaneous accumulation of ssDNA with no fork stalling, indicative of an uncoupling of leading and lagging strands promoted by the steady progression of POLE1 together with the CMG (Figure 7A). Although POLA1 is also required for priming of the leading strand when origins fire, we interpret the rapid increase of ssDNA upon PolAi as arising mostly at the lagging strand of

already active forks, given the relatively small number of newly fired forks within the experimental conditions used in this study. Moreover, it is unclear whether inhibition of POLA1 at the leading strand would rather cause replisomes to stall. ssDNA increase is much lower when POLD1 is depleted, probably because priming is the limiting step in lagging strand synthesis. POLE1 depletion, in contrast, slightly reduced the levels of basal ssDNA, supporting that the uncoupling of the replicative helicase on the leading strand is relatively rather contained *in vivo* (Zellweger et al., 2015). Also consistent is the striking difference in ssDNA generation between PolAi and HU/APH (Figure 3A).

The fact that cells with limited POLA1 activity can proliferate with sustainably elevated ssDNA levels (and not exhaust the RPA pool) shows that replication forks can operate with an unexpected degree of plasticity. It implies that larger ssDNA loops can accumulate at the lagging strand and that the extra delay at the priming step is compensated by POLD polymerizing faster than POLE (Figure 7B; Pandey et al., 2009). This would be consistent with *in vitro* data showing that the speed of the leading strand polymerase is restrained by the replicative helicase (Stano et al., 2005).

When POLA1 is inhibited, replication forks can virtually unzip the parental DNA at a high speed, leaving one strand unreplicated and causing a rapid RPA exhaustion. RC has been previously associated with the use of inhibitors of ATR and CHK1 kinases and the premature activation of mitotic endonucleases (such as MUS81) due to the rise in CDK levels in S-phase (reviewed in Toledo et al., 2017). However, our data now demonstrate that RC is a lethal event linked exclusively to insufficient ssDNA protection during DNA replication (Figure 5C).

Our data suggest that an uncoordinated mode of replication between strands has been favored and conserved across kingdoms as the most efficient solution for bidirectional DNA synthesis (Graham et al., 2017). Allowing leading and lagging strand synthesis to work independently, the cell relies on a very efficient and stochastic priming machinery to ensure the duplication of the lagging strand by "filling all gaps" behind the replisome. Thus, we propose that although uncoupling prone, this mechanism of DNA replication has been optimized to keep actual events of strand uncoupling rare and likely evolved to allow a minimum OF size that facilitates an efficient processing of OFs in coordination with nucleosome size (Smith and Whitehouse, 2012). Yet, supporting that uncoupling can happen, ssDNA track lengths detected in mammalian cells show an unusual variability (Zellweger et al., 2015). Overall, proliferating cells show a significant amount of CB-RPA linked to DNA replication (Figure 5A), and we can speculate that cells have evolved a surplus of RPA as a safety measure to complement the lack of an active ssDNA-limiting mechanism (Toledo et al., 2013). Additionally, the checkpoint machinery must tolerate the accumulation of ssDNA at forks if this is part of their normal functioning (see below). These aspects enable cells to proliferate with supraphysiological levels of ssDNA (Figure 6).

Using PolAi has offered us the possibility to dissect the specific role of ssDNA formation in ATR signaling *in vivo* without using classical RS inducers. Previous studies using *Xenopus laevis* extracts had shown that ssDNA is not sufficient to trigger a stress response but works as an amplifier of ATR signaling (Byun et al., 2005; MacDougall et al., 2007). These observations were done using plasmids simulating ssDNA-containing replication intermediates, and our study takes a leap forward by confirming them on fully functional replication forks *in vivo* (Figure 7C). This suggests that other events related to fork stalling are key in triggering a stress response, whereas active forks (regardless of the ssDNA load) are refractory to do so. This distinction has been a topic of discussion because active forks have *a priori* the same molecular requirements for ATR activation as a stalled fork, namely ssDNA (at the lagging strand) and a 5′ end junction to recruit TOPBP1 and the 9-1-1 complex (MacDougall et al., 2007; Majka et al., 2006). Our work shows that additional ssDNA is not required to activate a stress response, in agreement with the accepted model where ATR and TOPBP1 interact at a 5′ dsDNA-ssDNA junction (Cimprich and Cortez, 2008). Yet, how 5′ junctions turn "competent" for ATR activation after fork stalling is still a matter of debate (Cimprich and Cortez, 2008). It is possible that signaling at active forks is hindered because 5′ ends are occupied by RNA, which could affect the recruitment of the 9-1-1 complex, or maybe these ends are simply too transient unless polymerases are stalled. POLA1 was shown to be involved in ATR signaling by the recruitment of the 9-1-1 complex (Delacroix et al., 2007) and primer synthesis (Byun et al., 2005; Van et al., 2010), similarly to POLK (Bétous et al., 2013). However, inhibition of POLA1 together with RS enhances CHK1 phosphorylation rather than suppressing it (Figure 4E). This is likely due to the increase in ssDNA caused by PolAi but also suggests that POLA1 activity is not essential for ATR signaling *in vivo*. We hope that our data on the use of PolAi *in vivo* encourage further studies to clarify these important aspects of DNA replication.

ssDNA formation has been largely viewed as a pathological event linked to RS (Zeman and Cimprich, 2014). However, it is also a natural requirement for OF synthesis, and thus, it is logical that cells have evolved to tolerate ssDNA and not trigger a checkpoint response during physiological DNA replication. This could explain that CHK1 phosphorylation is largely independent of ETAA1 (Figure 5; Bass et al., 2016; Haahr et al., 2016), which otherwise, by its ability to activate ATR directly on RPA-coated ssDNA, could have a severe impact on CDK activity during normal OF synthesis. Yet, the physiological levels of ssDNA might still modulate CHK1 activity in unstressed conditions, where ATR/ATRIP is still recruited to RPA (Figure 4). This intrinsic activity has been recently shown essential to limit CDK activity in S-phase (Saldivar et al., 2018). As CHK1 phosphorylation is largely TOPBP1 dependent (Figure 4E), it is still unclear how then the intrinsic checkpoint is regulated. Potentially, there could be some basal ATR-TOPBP1 interaction at unstressed forks (Figure 7C), although a recent report proposed that stochastic fork stalling events regulate the endogenous ATR activity and CDK levels in S-phase (Daigh et al., 2018). Further studies will be necessary to clarify these important aspects of the ATR signaling pathway.

Our results indicate that RC caused by strand uncoupling explains the cytotoxic properties of ST1926, which has been tested as an anticancer agent in preclinical studies but only with modest

results (Aouad et al., 2017; Basma et al., 2016; Karam et al., 2018). In this regard, our data open opportunities for enhancing the antitumoral effect of both PolAi and ATR/CHK1 inhibitors, which are already in clinical trials. Although the development of novel and more potent PolAis might be necessary for clinical applications, we also entertain the idea that other lagging strand regulators might be druggable, a possibility that seems worthwhile pursuing.

STAR★METHODS

Detailed methods are provided in the online version of this paper and include the following:

- KEY RESOURCES TABLE
- LEAD CONTACT AND MATERIALS AVAILABILITY
- EXPERIMENTAL MODEL AND SUBJECT DETAILS
  - Cell lines
  - *Xenopus* egg extracts
- METHOD DETAILS
  - Drugs and Cell culture Supplements
  - Gene silencing by siRNA
  - Sequencing
  - Immunostaining
  - Detection of ultrafine anaphase bridges (UFB)
  - Preparation and staining of DNA Fibers
  - Microscopy and QIBC
  - Processing of Time-Lapse Images
  - Immunofluorescence staining procedure for Structured Illumination Microscopy (SIM)
  - Image acquisition, reconstruction and analysis for SIM
  - Chromatin fractionation
  - Immunoblotting
  - Egg extract and chromatin binding
  - Electron microscopy (EM)
  - Clonogenic and survival assays
- QUANTIFICATION AND STATISTICAL ANALYSIS
- DATA AND CODE AVAILABILITY

SUPPLEMENTAL INFORMATION

Supplemental Information can be found online at https://doi.org/10.1016/j.celrep.2020.01.067.

ACKNOWLEDGMENTS

We thank Deepak Nijhawan (University of Texas Southwestern) for the CD437-resistant cell lines; Dr. F. Javier Piedrafita (San Diego State University) for the compounds MX3350-1 and MX781; Maj-Britt Rask and Dr. Claudia Lukas (University of Copenhagen) for the RPA2-EGFP/PCNA-mCherry-expressing cells; Dr. Peter Haahr and Dr. Niels Mailand for the ETAA1-overexpressing cell lines; and Dr. Veronique Smits for the GFP fusion constructs of ATRIP, RAD9, RAD1, and HUS1. We thank all members of the Toledo Laboratory, Dr. Andrés López-Contreras, Dr. Julien Duxin, Dr. Kai Neelsen, Dr. Ian Hickson, and Dr. Peter Haahr (University of Copenhagen) for valuable feedback on the manuscript. This work was supported by the European Research Council, European Union (ERC-StG-679754 to L.T. and ERC-ConG-614541 to V.C.), the Danish National Research Foundation, Denmark (DNRF115), and the Novo Nordisk Foundation, Denmark (NNF14CC0001).

AUTHOR CONTRIBUTIONS

A.E., J.B., S.A., G.Z., and L.T. designed, performed, and analyzed most of the experiments. G.B. carried out EM microscopy supervised by V.C. F.O. carried out SIM imaging, and K.S. contributed with DNA fiber experiments and IOD analysis. J.L. provided critical input and advice during the development of the project. L.T. conceived, designed, and supervised the study. L.T. and A.E. wrote the manuscript. All of the authors read, edited, and commented on the manuscript.

DECLARATION OF INTERESTS

The authors declare no competing interests.

Received: May 14, 2019
Revised: December 17, 2019
Accepted: January 22, 2020
Published: February 18, 2020

REFERENCES

Abdel-Samad, R., Aouad, P., Gali-Muhtasib, H., Sweidan, Z., Hmadi, R., Kadara, H., D'Andrea, E.L., Fucci, A., Pisano, C., and Darwiche, N. (2018). Mechanism of action of the atypical retinoid ST1926 in colorectal cancer: DNA damage and DNA polymerase α. Am. J. Cancer Res. *8*, 39–55.

Anglana, M., Apiou, F., Bensimon, A., and Debatisse, M. (2003). Dynamics of DNA replication in mammalian somatic cells: nucleotide pool modulates origin choice and interorigin spacing. Cell *114*, 385–394.

Aouad, P., Saikali, M., Abdel-Samad, R., Fostok, S., El-Houjeiri, L., Pisano, C., Talhouk, R., and Darwiche, N. (2017). Antitumor activities of the synthetic retinoid ST1926 in two-dimensional and three-dimensional human breast cancer models. Anticancer Drugs *28*, 757–770.

Ball, G., Demmerle, J., Kaufmann, R., Davis, I., Dobbie, I.M., and Schermelleh, L. (2015). SIMcheck: a Toolbox for Successful Super-resolution Structured Illumination Microscopy. Sci. Rep. *5*, 15915.

Basma, H., Ghayad, S.E., Rammal, G., Mancinelli, A., Harajly, M., Ghamloush, F., Dweik, L., El-Eit, R., Zalzali, H., Rabeh, W., et al. (2016). The synthetic retinoid ST1926 as a novel therapeutic agent in rhabdomyosarcoma. Int. J. Cancer *138*, 1528–1537.

Bass, T.E., Luzwick, J.W., Kavanaugh, G., Carroll, C., Dungrawala, H., Glick, G.G., Feldkamp, M.D., Putney, R., Chazin, W.J., and Cortez, D. (2016). ETAA1 acts at stalled replication forks to maintain genome integrity. Nat. Cell Biol. *18*, 1185–1195.

Bétous, R., Pillaire, M.J., Pierini, L., van der Laan, S., Recolin, B., Ohl-Séguy, E., Guo, C., Niimi, N., Grúz, P., Nohmi, T., et al. (2013). DNA polymerase κ-dependent DNA synthesis at stalled replication forks is important for CHK1 activation. EMBO J. *32*, 2172–2185.

Bizard, A.H., Nielsen, C.F., and Hickson, I.D. (2018). Detection of Ultrafine Anaphase Bridges. Methods Mol. Biol. *1672*, 495–508.

Boos, D., Yekezare, M., and Diffley, J.F.X. (2013). Identification of a heteromeric complex that promotes DNA replication origin firing in human cells. Science *340*, 981–984.

Byun, T.S., Pacek, M., Yee, M.C., Walter, J.C., and Cimprich, K.A. (2005). Functional uncoupling of MCM helicase and DNA polymerase activities activates the ATR-dependent checkpoint. Genes Dev. *19*, 1040–1052.

Chan, K.L., Palmai-Pallag, T., Ying, S., and Hickson, I.D. (2009). Replication stress induces sister-chromatid bridging at fragile site loci in mitosis. Nat. Cell Biol. *11*, 753–760.

Cimprich, K.A., and Cortez, D. (2008). ATR: an essential regulator of genome integrity. Nat. Rev. Mol. Cell Biol. *9*, 616–627.

Daigh, L.H., Liu, C., Chung, M., Cimprich, K.A., and Meyer, T. (2018). Stochastic Endogenous Replication Stress Causes ATR-Triggered Fluctuations in CDK2 Activity that Dynamically Adjust Global DNA Synthesis Rates. Cell Syst. *7*, 17–27.e3.

Delacroix, S., Wagner, J.M., Kobayashi, M., Yamamoto, K., and Karnitz, L.M. (2007). The Rad9-Hus1-Rad1 (9-1-1) clamp activates checkpoint signaling via TopBP1. Genes Dev. *21*, 1472–1477.

Demmerle, J., Innocent, C., North, A.J., Ball, G., Müller, M., Miron, E., Matsuda, A., Dobbie, I.M., Markaki, Y., and Schermelleh, L. (2017). Strategic and practical guidelines for successful structured illumination microscopy. Nat. Protoc. *12*, 988–1010.

Gan, H., Yu, C., Devbhandari, S., Sharma, S., Han, J., Chabes, A., Remus, D., and Zhang, Z. (2017). Checkpoint Kinase Rad53 Couples Leading- and Lagging-Strand DNA Synthesis under Replication Stress. Mol. Cell *68*, 446–455.e3.

Graham, J.E., Marians, K.J., and Kowalczykowski, S.C. (2017). Independent and Stochastic Action of DNA Polymerases in the Replisome. Cell *169*, 1201–1213.e17.

Haahr, P., Hoffmann, S., Tollenaere, M.A.X., Ho, T., Toledo, L.I., Mann, M., Bekker-Jensen, S., Räschle, M., and Mailand, N. (2016). Activation of the ATR kinase by the RPA-binding protein ETAA1. Nat. Cell Biol. *18*, 1196–1207.

Han, T., Goralski, M., Capota, E., Padrick, S.B., Kim, J., Xie, Y., and Nijhawan, D. (2016). The antitumor toxin CD437 is a direct inhibitor of DNA polymerase α. Nat. Chem. Biol. *12*, 511–515.

Hashimoto, Y., Ray Chaudhuri, A., Lopes, M., and Costanzo, V. (2010). Rad51 protects nascent DNA from Mre11-dependent degradation and promotes continuous DNA synthesis. Nat. Struct. Mol. Biol. *17*, 1305–1311.

Jackson, D.A., and Pombo, A. (1998). Replicon clusters are stable units of chromosome structure: evidence that nuclear organization contributes to the efficient activation and propagation of S phase in human cells. J. Cell Biol. *140*, 1285–1295.

Karam, L., Houshaymi, B., Abdel-Samad, R., Jaafar, M., Halloum, I., Pisano, C., Neipel, F., Darwiche, N., and Abou Merhi, R. (2018). Antitumor activity of the synthetic retinoid ST1926 on primary effusion lymphoma in vitro and in vivo models. Oncol. Rep. *39*, 721–730.

Kraus, F., Miron, E., Demmerle, J., Chitiashvili, T., Budco, A., Alle, Q., Matsuda, A., Leonhardt, H., Schermelleh, L., and Markaki, Y. (2017). Quantitative 3D structured illumination microscopy of nuclear structures. Nat. Protoc. *12*, 1011–1028.

Kumagai, A., Lee, J., Yoo, H.Y., and Dunphy, W.G. (2006). TopBP1 activates the ATR-ATRIP complex. Cell *124*, 943–955.

Lee, J.B., Hite, R.K., Hamdan, S.M., Xie, X.S., Richardson, C.C., and van Oijen, A.M. (2006). DNA primase acts as a molecular brake in DNA replication. Nature *439*, 621–624.

Lukas, C., Savic, V., Bekker-Jensen, S., Doil, C., Neumann, B., Pedersen, R.S., Grøfte, M., Chan, K.L., Hickson, I.D., Bartek, J., and Lukas, J. (2011). 53BP1 nuclear bodies form around DNA lesions generated by mitotic transmission of chromosomes under replication stress. Nat. Cell Biol. *13*, 243–253.

MacDougall, C.A., Byun, T.S., Van, C., Yee, M.C., and Cimprich, K.A. (2007). The structural determinants of checkpoint activation. Genes Dev. *21*, 898–903.

Majka, J., Binz, S.K., Wold, M.S., and Burgers, P.M.J. (2006). Replication protein A directs loading of the DNA damage checkpoint clamp to 5′-DNA junctions. J. Biol. Chem. *281*, 27855–27861.

Minocherhomji, S., Ying, S., Bjerregaard, V.A., Bursomanno, S., Aleliunaite, A., Wu, W., Mankouri, H.W., Shen, H., Liu, Y., and Hickson, I.D. (2015). Replication stress activates DNA repair synthesis in mitosis. Nature *528*, 286–290.

O'Donnell, M., Langston, L., and Stillman, B. (2013). Principles and concepts of DNA replication in bacteria, archaea, and eukarya. Cold Spring Harb. Perspect. Biol. *5*, a010108.

Okazaki, R. (1967). [Molecular mechanism of DNA synthesis]. Tanpakushitsu Kakusan Koso *12*, 795–805.

Pagès, V., and Fuchs, R.P. (2003). Uncoupling of leading- and lagging-strand DNA replication during lesion bypass in vivo. Science *300*, 1300–1303.

Pandey, M., Syed, S., Donmez, I., Patel, G., Ha, T., and Patel, S.S. (2009). Coordinating DNA replication by means of priming loop and differential synthesis rate. Nature *462*, 940–943.

Pérez-Rodríguez, S., Ortiz, M.A., Pereira, R., Rodríguez-Barrios, F., de Lera, A.R., and Piedrafita, F.J. (2009). Highly twisted adamantyl arotinoids: synthesis, antiproliferative effects and RXR transactivation profiles. Eur. J. Med. Chem. *44*, 2434–2446.

Saldivar, J.C., Hamperl, S., Bocek, M.J., Chung, M., Bass, T.E., Cisneros-Soberanis, F., Samejima, K., Xie, L., Paulson, J.R., Earnshaw, W.C., et al. (2018). An intrinsic S/G_2 checkpoint enforced by ATR. Science *361*, 806–810.

Sannino, V., Pezzimenti, F., Bertora, S., and Costanzo, V. (2017). Xenopus laevis as Model System to Study DNA Damage Response and Replication Fork Stability. Methods Enzymol. *591*, 211–232.

Smith, D.J., and Whitehouse, I. (2012). Intrinsic coupling of lagging-strand synthesis to chromatin assembly. Nature *483*, 434–438.

Somyajit, K., Gupta, R., Sedlackova, H., Neelsen, K.J., Ochs, F., Rask, M.B., Choudhary, C., and Lukas, J. (2017). Redox-sensitive alteration of replisome architecture safeguards genome integrity. Science *358*, 797–802.

Sparks, J.L., Chistol, G., Gao, A.O., Räschle, M., Larsen, N.B., Mann, M., Duxin, J.P., and Walter, J.C. (2019). The CMG Helicase Bypasses DNA-Protein Cross-Links to Facilitate Their Repair. Cell *176*, 167–181.e21.

Stano, N.M., Jeong, Y.J., Donmez, I., Tummalapalli, P., Levin, M.K., and Patel, S.S. (2005). DNA synthesis provides the driving force to accelerate DNA unwinding by a helicase. Nature *435*, 370–373.

Syljuåsen, R.G., Sørensen, C.S., Hansen, L.T., Fugger, K., Lundin, C., Johansson, F., Helleday, T., Sehested, M., Lukas, J., and Bartek, J. (2005). Inhibition of human Chk1 causes increased initiation of DNA replication, phosphorylation of ATR targets, and DNA breakage. Mol. Cell. Biol. *25*, 3553–3562.

Taylor, M.R.G., and Yeeles, J.T.P. (2018). The Initial Response of a Eukaryotic Replisome to DNA Damage. Mol. Cell *70*, 1067–1080.e12.

Taylor, M.R.G., and Yeeles, J.T.P. (2019). Dynamics of Replication Fork Progression Following Helicase-Polymerase Uncoupling in Eukaryotes. J. Mol. Biol. *431*, 2040–2049.

Toledo, L.I., Altmeyer, M., Rask, M.B., Lukas, C., Larsen, D.H., Povlsen, L.K., Bekker-Jensen, S., Mailand, N., Bartek, J., and Lukas, J. (2013). ATR prohibits replication catastrophe by preventing global exhaustion of RPA. Cell *155*, 1088–1103.

Toledo, L., Neelsen, K.J., and Lukas, J. (2017). Replication Catastrophe: When a Checkpoint Fails because of Exhaustion. Mol. Cell *66*, 735–749.

Van, C., Yan, S., Michael, W.M., Waga, S., and Cimprich, K.A. (2010). Continued primer synthesis at stalled replication forks contributes to checkpoint activation. J. Cell Biol. *189*, 233–246.

Walter, J., and Newport, J. (2000). Initiation of eukaryotic DNA replication: origin unwinding and sequential chromatin association of Cdc45, RPA, and DNA polymerase alpha. Mol. Cell *5*, 617–627.

Warmerdam, D.O., Kanaar, R., and Smits, V.A.J. (2010). Differential Dynamics of ATR-Mediated Checkpoint Regulators. J. Nucleic Acids *2010*, 319142.

Yao, N.Y., Georgescu, R.E., Finkelstein, J., and O'Donnell, M.E. (2009). Single-molecule analysis reveals that the lagging strand increases replisome processivity but slows replication fork progression. Proc. Natl. Acad. Sci. USA *106*, 13236–13241.

Zellweger, R., Dalcher, D., Mutreja, K., Berti, M., Schmid, J.A., Herrador, R., Vindigni, A., and Lopes, M. (2015). Rad51-mediated replication fork reversal is a global response to genotoxic treatments in human cells. J. Cell Biol. *208*, 563–579.

Zeman, M.K., and Cimprich, K.A. (2014). Causes and consequences of replication stress. Nat. Cell Biol. *16*, 2–9.

Zou, L., and Elledge, S.J. (2003). Sensing DNA damage through ATRIP recognition of RPA-ssDNA complexes. Science *300*, 1542–1548.

STAR★METHODS

KEY RESOURCES TABLE

REAGENT or RESOURCE	SOURCE	IDENTIFIER
Antibodies		
Rabbit polyclonal anti-53BP1	Novus Biologicals	Cat# NB100-305; RRID:AB_10001695
Mouse monoclonal anti-β-actin [clone C4]	Santa Cruz	Cat# sc-47778; RRID:AB_2714189
Rabbit polyclonal anti-BLM	Abcam	Cat# ab2179; RRID:AB_2290411
Mouse monoclonal anti-BrdU [clone B44] *(for BrdU and IdU detection)*	BD Bioscience	Cat# 347580; RRID:AB_10015219
Rat monoclonal anti-BrdU [clone BU1/75 (ICR1)] *(for CldU detection)*	Abcam	Cat# ab6326; RRID:AB_305426
Rabbit polyclonal anti-ssDNA	Tecan/IBL International	Cat# 18731; RRID:AB_494649
Rabbit monoclonal anti-CHK1-S345P (This antibody was used to detect *Xenopus* CHK1-S344P)	Cell signaling	Cat# 2348; RRID:AB_331212
Sheep polyclonal anti-ETAA1	Laboratory of Niels Mailand	https://www.ncbi.nlm.nih.gov/pubmed/27723717
Mouse monoclonal anti-MCM3 [clone E-8]	Santa Cruz	Cat# sc-390480
Rabbit polyclonal anti-DNA polymerase alpha (PolA1)	Abcam	Cat# ab31777; RRID:AB_731976
Rat monoclonal anti-p48 Primase (Prim1) [clone 8G109]	Cell signaling	Cat# 4725; RRID:AB_823688
Rabbit polyclonal anti-RPA	Custom made	N/A
Rabbit monoclonal anti-RPA1 [clone EPR2472]	Abcam	Cat# ab79398; RRID:AB_1603759
Mouse monoclonal anti-RPA2 [clone 9H8]	Novus Biologicals	Cat# NB600-565; RRID:AB_10003312
Rabbit polyclonal anti-TopBP1	Bethyl Laboratories	Cat# A300-111A; RRID:AB_2272050
Mouse monoclonal anti-γH2AX (clone JBW301)	Millipore	Cat# 05-636; RRID:AB_309864
CDC45	Santa Cruz	sc-55569; RRID:AB_831146
PCNA	Santa Cruz	sc-56; RRID:AB_628110
GINS3	Bethyl Laboratories	A304-124A; RRID:AB_2621373
HIST3	Abcam	ab1791; RRID:AB_302613
PolD1	Abcam	ab10362; RRID:AB_297099
PolE	Abcam	ab134941
Rabbit polyclonal anti-*Xenopus* Orc1	Laboratory of Vincenzo Costanzo	https://www.ncbi.nlm.nih.gov/pubmed/27111843
Mouse monoclonal anti-*Xenopus* Mcm7	Santa Cruz	Cat# sc-9966; RRID:AB_627235
Rabbit polyclonal anti-*Xenopus* RPA1	Laboratory of Jean Gautier	https://www.ncbi.nlm.nih.gov/pmc/articles/PMC5594205/
Mouse Monoclonal anti-*Xenopus* Pol δ 125 kDa	Laboratory of Vincenzo Costanzo	Abmart: clone 19570-1-1/C316 https://www.ncbi.nlm.nih.gov/pmc/articles/PMC5594205/
Biological samples		
Xenopus laevis egg extracts	This study	N/A
Chemicals, Peptides, and Recombinant Proteins		
HU (Hydroxyurea)	Sigma-Aldrich	Cat# H8627
APH (Aphidicolin from Nigrospora sphaerica)	Sigma-Aldrich	Cat# A0781
CD437	Sigma-Aldrich	Cat# C5865
ST1926 (Adarotene)	MedChemExpress	Cat# HY-14808
MX3350	F. J. Piedrafita	N/A
Adapalene	Santa Cruz	Cat# sc-203803
CD2665	Santa Cruz	Cat# sc-293988
MX781	F. J. Piedrafita	N/A
CD1530	TOCRIS Bioscience	Cat# 2554

(*Continued on next page*)

Continued

REAGENT or RESOURCE	SOURCE	IDENTIFIER
AZ20 (ATRi)	Selleckchem	Cat# S7050
AZD7762 (Chk1i)	Selleckchem	Cat# S1532
RO8803 (CDK1i)	MedChemExpress	Cat# HY-12529
CDK2 inhibitor II (CDK2i)	BioNordika	Cat# 15154
PHA-767491 (PHA 767491 hydrochloride) (CDC7i)	Sigma-Aldrich	Cat# PZ0178
Thymidine	Sigma-Aldrich	Cat# T1895
BrdU (5-Bromo-2′-deoxyuridine)	Sigma-Aldrich	Cat# B5002
CldU (5-Chloro-2′-deoxyuridine)	Sigma-Aldrich	Cat# C6891
IdU (5-Iodo-2′-deoxyuridine)	Sigma-Aldrich	Cat# I7125
EdU (5-Ethynyl-2′-deoxyuridine)	Sigma-Aldrich	Cat# T511285
DMSO (Dimethyl sulfoxide)	Sigma-Aldrich	Cat# D8418
BSA (Bovine serum Albumin)	Sigma-Aldrich	Cat# A7906
DTT (DL-Dithiothreitol)	Sigma-Aldrich	Cat# D0632
β-Mercaptoethanol	Sigma-Aldrich	Cat# M6250
Crystal violet	Sigma-Aldrich	Cat# C0775
Formaldehyde 4%	VWR	Cat# 9713.1000
Formaldehyde 4%	EM grade, Polysciences	Cat# 00380-250
DAPI (Diamidino-2-Phenylindole Dihydrochloride)	Sigma-Aldrich	Cat# D9542
Mowiol® 4-88	Sigma-Aldrich	Cat# 81381
Vectashield®	Vectorlabs	Cat# H-1000
TMP (4,5′,8-Trimethylpsoralen)	Sigma-Aldrich	Cat# T6137
Chorionic gonadotropin	Sigma-Aldrich	Cat# CL10
Spermine	Sigma-Aldrich	Cat# S3256
Spermidine	Sigma-Aldrich	Cat# S2626
Lysolecithin	Sigma-Aldrich	Cat# L1381
Calcium ionophore	Sigma-Aldrich	Cat# A23187
Proteinase K	Sigma-Aldrich	Cat# 3115887001
RNase A	Thermo Fischer Scientific	Cat# EN0531
Alexa Fluor 647 Azide, Triethylammonium Salt	Life Technologies	Cat# A10277
Benzonase® Nuclease	Sigma-Aldrich	Cat# E1014-25KU
Vent® DNA Polymerase	New England Biolabs	Cat# M0254S
Critical Commercial Assays		
DNeasy Blood & Tissue Kit	QIAGEN	Cat# 69504
NucleoSpin® Gel and PCR Clean-up	AH Diagnostics	Cat# 740609.50
Experimental Models: Cell Lines		
Human: U2OS	ATCC	HTB-96
Human: hTERT-RPE1	ATCC	CRL-4000
Human: Super-RPA #3 U2OS	Toledo Laboratory	N/A
Human: U2OS/H2B-EGFP	Toledo Laboratory	N/A
Human: U2OS/RPA2-EGFP	Toledo Laboratory	N/A
Human: U2OS/RPA2-EGFP/PCNA-mCHerry	Jiri Lukas Laboratory	N/A
Human: U2OS/ETAA1-GFP	Laboratory of Niels Mailand	https://www.ncbi.nlm.nih.gov/pubmed/27723717
Human: U2OS/ATRIP-EGFP	Toledo Laboratory	N/A
Human: U2OS/RAD1-EGFP	Toledo Laboratory	N/A
Human: U2OS/RAD9-EGFP	Toledo Laboratory	N/A
Human: HCT116 *wild-type*	Laboratory of Deepak Nijhawan	https://www.ncbi.nlm.nih.gov/pmc/articles/PMC4912453/

(*Continued on next page*)

Continued

REAGENT or RESOURCE	SOURCE	IDENTIFIER
Human: HCT116 *PolA1 mutant (L764S)*	Laboratory of Deepak Nijhawan	https://www.ncbi.nlm.nih.gov/pmc/articles/PMC4912453/
Human: HeLa *wild-type*	Laboratory of Deepak Nijhawan	https://www.ncbi.nlm.nih.gov/pmc/articles/PMC4912453/
Human: HeLa *PolA1 mutant (A765M)*	Laboratory of Deepak Nijhawan	https://www.ncbi.nlm.nih.gov/pmc/articles/PMC4912453/
Human: A549	Laboratory of Ian Hickson	N/A
Human: SW39	Laboratory of Ian Hickson	N/A
Human: HT1080	Laboratory of Ian Hickson	N/A
Human: WI-38	Laboratory of Ian Hickson	N/A
Experimental Models: *Xenopus* egg extracts		
Xenopus laevis females	Nasco	Cat# LM00535MX
Xenopus laevis males	Nasco	Cat# LM00715MX
Oligonucleotides		
See Table S1 for siRNA duplexes	This paper	N/A
Primer P1 (POLA1 exon 21 forward): *AGCATTGGG ATCAGTGGTATG*	This paper	https://www.ncbi.nlm.nih.gov/pmc/articles/PMC4912453/
Primer P2 (POLA1 exon 21 reverse): *TGTAAAACG ACGGCCAGTTCTCCCAACCAGTTCTTCCT*	This paper	https://www.ncbi.nlm.nih.gov/pmc/articles/PMC4912453/
Software and Algorithms		
Fiji (ImageJ)	NIH	https://imagej.nih.gov/ij/docs/guide/146-2.html
ScanR acquisition software	Olympus	https://www.olympus-lifescience.com/en/microscopes/inverted/scanr/#!
ScanR analysis software	Olympus	https://www.olympus-lifescience.com/en/microscopes/inverted/scanr/#!
TIBCO Spotfire	Perkin Elmer	https://www.perkinelmer.com/product/tibco-spotfire-in-research-spotfirer
Stackreg/Turboreg plugin	Ecole polytechnique federale de lausanne	http://bigwww.epfl.ch/thevenaz/stackreg/
ZEISS black, 2.3 SP1	ZEISS	N/A
Gatan Micrograph software	Gatan	N/A
GraphPad Prism 7.0.	GraphPad	https://www.graphpad.com/scientific-software/prism/
Affinity Photo	Affinity	https://affinity.serif.com/en-gb/photo/
Affinity Designer	Affinity	https://affinity.serif.com/en-gb/designer/
Other		
DharmaFECT^{TM} siRNA transfection reagents	VWR	Cat# T-2001-03
96-well microplates (CELL CULTURE MICROPLATE, 96 WELL, PS, F-BOTTOM (8 × 4, 32 stk/pack))	Greiner-BIO	Cat# GR-655090
No. 1.5 coverslips	Marienfeld	Cat# 0107032
Protease inhibitor tablets (cOmplete ULTRA Tablets, Mini, EASYpack Protease Inhibitor Cocktail)	Roche	Cat# 000000005892970001
Phosphatase inhibitor tablets (PhosSTOP; cOmplete ULTRA Tablets, Mini, EASYpack)	Roche	Cat# 000000004906837001
TetraSpeck beads	Invitrogen	Cat# T7280

LEAD CONTACT AND MATERIALS AVAILABILITY

This study did not generate new unique reagents. Further information and requests for resources and reagents should be directed to and will be fulfilled by the Lead Contact, Luis Ignacio Toledo (ltoledo@sund.ku.dk).

EXPERIMENTAL MODEL AND SUBJECT DETAILS

Cell lines

All experiments were performed in U2OS cells unless specified otherwise. Asynchronous cell populations were used in all cases. U2OS (female) and hTERT-RPE1 (female) were obtained from ATCC. U2OS cells stably expressing AcGFP-RPA3-P2A-RPA1-P2A-RPA2 (Super-RPA U2OS) and RPA2 fused to EGFP (U2OS/RPA2-EGFP) were previously published (Toledo et al., 2013). H2B fused to EGFP was stably expressed in U2OS by lentiviral infection (U2OS/H2B-EGFP). Cells expressing RPA2 fused to EGFP and PCNA fused to mCherry were stably expressed by plasmid integration (U2OS/RPA2-EGFP/PCNA-mCherry). U2OS cells stably expressing a siRNA resistant (sequence #4) ETAA1 variant fused to GFP (U2OS/ ETAA1-GFP) were a kind gift of P. Haahr and Niels Mailand (Center for Protein Research, University of Copenhagen, Denmark). Polyclonal U2OS stably expressing ATRIP-EGFP, RAD9-EGFP and RAD1-EGFP were obtained by transient transfection and antibiotic selection. HCT116 (male; *wild-type* (*wt)* and *PolA1 mutant*) and HeLa (female; wt and *PolA1 mutant*) cells were a kind gift from Deepak Nijhawan. A549 (male), SW39 (female), HT1080 (male) and WI-38 (female) were provided by Ian Hickson (Center for Chromosomal Stability, University of Copenhagen, Denmark). The cell lines were not authenticated. All cell lines were cultured at 37C in DMEM, supplemented with 6% fetal bovine serum (FBS) and Penicillin-Streptomycin (10,000 U/mL) all from Thermo Fisher Scientific. Cells were monthly verified to be free of mycoplasma contamination.

Xenopus egg extracts

Eggs derived from *Xenopus laevis* female frogs were harvested in a non-invasive way following chorionic gonadotropin (Sigma, CG10) injections. Surgical procedures were occasionally performed on male frogs to collect sperm nuclei. All the protocols were approved by IFOM Animal Welfare committee and the Italian Ministry of Health. The number of animals used was kept to a minimum. The animals were maintained in highly regulated and monitored conditions with room and water temperature at 19C. Basic husbandry requirements were provided by the *Xenopus* facility at IFOM.

METHOD DETAILS

Drugs and Cell culture Supplements

HU (Sigma-Aldrich), APH (Sigma-Aldrich), CD437 (Sigma-Aldrich), ST1926 (MedchemExpress), MX3350 (F.J.Piedrafita), Adapalene (Santa Cruz), CD2665 (Santa Cruz), MX781 (F.J.Piedrafita), CD1530 (TOCRIS Bioscience), ATRi (AZ20, Selleckchem), Chk1i (AZD7762, Selleckchem), CDK1i (RO3306, MedChemExpress), CDK2i (CDK2 inhibitor II, BioNordika) and CDC7i (PHA-767491, Sigma-Aldrich) were used as indicated in the corresponding figure legends. dNTP analogs Thymidine (10 M; Sigma-Aldrich), BrdU (10 M; Sigma-Aldrich), CldU (25 M; Sigma-Aldrich), IdU (250 M; Sigma-Aldrich) and EdU (10 M; Sigma-Aldrich) were used where indicated. DMSO (Sigma-Aldrich) was used, where indicated, at the same concentration as the drug used in parallel.

Gene silencing by siRNA

Transfections of siRNA duplexes were performed with DharmaFECT^{TM} (VWR) following manufacturer's guidelines. Unless specified otherwise, siRNAs were used at 10 nM and experiments were performed 48 h after transfection. In siRNA titration assays, total siRNA concentration was kept constant with the addition of CONTROL siRNA. A 1:1 mix of TIMELESS A and B, of POLD1 #14 and #15 and of ETAA1 #3 and ETAA1 #4 was used if not specified otherwise.

Sequencing

DNA from wt and *PolA1 mutant* HeLa cells was extracted using the DNeasy Blood & Tissue Kit (QIAGEN). The genomic region of POLA1 exon 21 targeted by CRISPR/Cas 9 was amplified in 30-cycle PCR reaction using Vent® DNA Polymerase (New England Biolabs). 50 ng of DNA input was used. The following primers were used at an annealing temperature of 58°C:

P1 (POLA1 exon 21 forward): AGCATTGGGATCAGTGGTATG
P2 (POLA1 exon 21 reverse): TGTAAAACGACGGCCAGT TTCTCCCAACCAGTTCTTCC

The PCR products were purified using NucleoSpin® Gel and PCR Clean-up Kit (AH Diagnostics) and sequenced by Sanger technology (Macrogen), using P2 as the sequencing primer.

Immunostaining

Cells growing on either 12 mm coverslips or 96-well microplates (Greiner-BIO) were fixed in formaldehyde 4% (VWR) for 15 min at room temperature (RT). Unless specified otherwise, pre-extraction was carried out before fixation by incubating the cells in 0.5% Triton X-100 PBS on ice for 1 min. When Click-it reactions were combined (EdU detection), these were performed prior to incubation with the primary antibodies. Click-it reaction was performed by incubating the fixed cells in Click-it buffer (100 mM Tris-HCl pH 8, 2 mM $CuSO_4$, 1 ng Alexa Fluor 647 Azide (Life Technologies), and 100 mM ascorbic acid for 30 min at RT.

Primary antibodies were diluted in filtered DMEM containing 6% FBS and 5% Bovine Serum Albumin (BSA). Incubations with the primary antibodies were performed at RT for 1 h. Coverslips/Plates were washed three times with 0.01% PBS-Tween20 and incubated in DMEM/FBS/BSA containing secondary fluorescently labeled antibodies (Alexa fluor® dyes (1/500; Life Technologies)) and DAPI (0.5 μg/ml; Sigma-Aldrich) for 1 h at RT. After two more washes in 0.01% PBS-Tween20, coverslips were dipped in distilled water, placed on 3MM paper to dry, and mounted on 6 μL Mowiol-based mounting media (Mowiol® 4-88/Glycerol/TRIS). For microplates, cells were directly imaged by adding filtered PBS after the washes.

Primary antibodies against the following proteins were used at the indicated dilutions: RPA (1/1000; Homemade), γH2AX (1/2000; Millipore) and 53BP1 (1/1000; Novus Biologicals).

Detection of ultrafine anaphase bridges (UFB)

Immunostaining of ultrafine anaphase bridges was performed as previously described in Bizard et al., (2018). Briefly, cells growing on 12 mm coverslips were rinsed with 1 mL of 1 × PBS. After that, cells were pre-extracted and fixed at RT by subsequent addition of 1 mL of pre-extraction Buffer A (0.2% Triton X-100, 20 mM PIPES pH 6.8, 1 mM $MgCl_2$, and 10 mM EGTA) and 2 mL of pre-extraction Buffer B (0.1% Triton X-100, 8% formaldehyde, 20 mM PIPES pH 6.8, 1 mM $MgCl_2$, and 10 mM EGTA) for 0.5 and 15 min respectively. Coverslips were then washed and cells were further permeabilized with PBS-AT (3% BSA, 0.5% Triton X-100 in 1 × PBS) at 4°C overnight (ON). The following day, coverslips were incubated with BLM antibody (1/200; Abcam) in PBS-AT at 4°C ON. Finally, coverslips were washed three times with PBS-AT and incubated with secondary fluorescently labeled antibody (Alexa fluor® dye (1/500; Life Technologies)) and DAPI (0.5 μg/ml; Sigma-Aldrich) in PBS-AT for 2 h at RT, washed 3 times with PBS-AT and mounted on 6 μL Mowiol-based mounting media (Mowiol® 4-88 (Sigma-Aldrich)/Glycerol/TRIS).

Preparation and staining of DNA Fibers

Cells were seeded at 10^5 confluency in 6-well plates and treated/pulse-labeled as indicated. Treated and labeled cells were harvested in ice-cold PBS and mixed 1:1 with unlabeled cells. Subsequently, 4 μL of the cell suspension was placed onto super-frost slides and mixed with 8 μL of lysis buffer (0.5% SDS, 200 mM Tris pH 7.5, 50 mM EDTA). After 2 min of incubation, slides were tilted at 15 to allow the cell lysate to flow along the slide slowly until the end of slide, air-dried for 10 min and then fixed in methanol:acetic acid (3:1) for 10min.

For CldU and IdU staining, slides were first rinsed 3 times in PBS, incubated with 2.5 M HCl for 80 min (denaturation) and washed four times in PBS (neutralization). After that, slides were blocked in blocking buffer (1x PBS, 0.1% Triton X-100, 1% BSA) for 30 min. CldU was detected by incubating slides with rat anti-BrdU antibody (1/200; Abcam; in blocking buffer) for 75 min at RT. Slides were then washed once with PBS containing 0.1% Tween20 followed by two times in PBS, fixed with formaldehyde 4% (VWR) and incubated with secondary fluorescently labeled antibodies (Alexa fluor® dyes (1/100; Life Technologies)) for 1h. Afterward, slides were washed with PBS, and IdU was detected using mouse anti-BrdU antibody (1/200; BD Bioscience) ON at 4°C and secondary fluorescently labeled antibodies (Alexa fluor® dyes (1/100; Life Technologies)) for 1h.

For IOD measurements, labeled cells were diluted 1/10 in non-labeled ones prior to fiber preparation. Anti-BrdU (1:100; Abcam) and Anti-ssDNA (1:500; Tecan/IBL International) antibodies were used. IOD distance was calculated measuring the distance between the center of 2 adjacent CldU labeled tracks.

Microscopy and QIBC

Coverslips were imaged using an Olympus IX-83 inverted microscope with an Olympus 63x oil objective. Images were analyzed using the Fiji (ImageJ) software. The number of cells analyzed in each experiment is specified in the corresponding figure legends.

Images of DNA Fibers were acquired using an Olympus IX-83 inverted microscope with an Olympus 63x oil objective. At least 250 fibers were counted in each condition. The track lengths were measured using the Fiji (ImageJ) software. Fork speed in kb/min was calculated where indicated by multiplying the measured length in μm with a conversion factor of 2.59 kb/μm and dividing by the duration of the labeling pulse (Jackson and Pombo, 1998).

Images used for QIBC were obtained automatically with the ScanR acquisition software controlling a motorized Olympus IX-83 wide-field microscope. The system was equipped with filter cubes compatible with DAPI, FITC, Cy3, and Cy5 fluorescent dyes, a Spectra X-LIGHT engine Illumination system with 6 color LEDs and emission filters, and a Hamamatsu Camera Orca Flash 4.0 V2. An Olympus Universal Plan Super Apo 10x Objective was used for all QIBC data. Images were processed using the ScanR image analysis software. TIBCO Spotfire® software was used to plot total nuclear pixel intensities for DAPI (Arbitrary units: A.U.) and mean (total pixel intensities divided by nuclear area) nuclear intensities (A.U.) for all other parameters (each of them specified in the corresponding figure legend) in color-coded scatter diagrams in a flow-cytometry-like fashion. Yellow dashed line indicates maximum CB-RPA levels in non-treated (NT) or CONTROL siRNA transfected cells unless specified otherwise. Likewise, TIBCO Spotfire software was used to analyze the percentages of RC and to measure the average nuclear intensities (A.U.) of the specified parameters (See figure legends). Green dashed line indicates max. CB-RPA levels in NT or CONTROL siRNA transfected cells unless specified otherwise.

Images of cells expressing RAD9/RAD1/ATRIP-GFP fusions were taken on the same Olympus IX83-ScanR system using an Olympus 60X silicone immersion objective (UPLSAPO60XS).

Live imaging was performed on the same Olympus IX83-ScanR system using an Olympus Plan Semi Apo 40x objective.

Processing of Time-Lapse Images

Images were imported into Fiji (ImageJ) and processed as stacks to generate output video files. Image composition and labeling was done in Fiji. In some cases, we enhanced the spatial visualization of dynamic intranuclear structures (like RPA foci) throughout the time-lapse by immobilizing cells '*in silico*'. For this we applied the Stackreg/Turboreg plugin (http://bigwww.epfl.ch/thevenaz/stackreg/) in Fiji as described before (Toledo et al., 2013).

Immunofluorescence staining procedure for Structured Illumination Microscopy (SIM)

SIM staining protocol was adapted from Kraus et al. (2017). In short, cells were grown to 80% confluency on 18x18 mm coverslips (No.1.5 coverslips Marienfeld Superior, 0.170+/− 0.005 mm, manually cleaned in 96% ethanol) in 6 well plastic plates. After treatment, coverslips were washed once in PBS, pre-extracted in ice-cold 0.2% PBS Triton X-100 and fixed in 4% formaldehyde (EM grade, Polysciences) for 10 min at RT. To prevent sample drying, PBS was added simultaneously when formaldehyde was aspired. Coverslips were washed once in PBS. Click-it reaction was performed (as explained above) before incubation with anti-RPA1 (1/500; Abcam) primary antibody, which was diluted in antibody diluent (DMEM medium containing 10% FBS and 0.05% sodium azide, filtered). Primary antibody incubations were performed in a dark chamber at RT for 1 h by pipetting 100 μL antibody solution per coverslip onto paramfilm and turning the coverslips into it. Afterward, coverslips were placed back in 6 well plates and were washed three times in PBS containing 0.2% Tween. Secondary antibody incubations were performed in a dark chamber at RT for 30 min and were supplemented with DAPI (0.5 μg/ml; Sigma-Aldrich) to stain DNA. Afterward, the samples were washed three times in PBS-Tween, once in distilled water to remove salt and dabbed on 3 MM paper. Samples were mounted without drying by turning into a 30 μL drop of non-hardening Vectashield® without DAPI (Vectorlabs, H-1000) on parafilm to ensure excess of mounting medium over water in the final sample in order to maintain the desired refractive index. Microscopy glass slides were manually cleaned in 96% ethanol and coverslips were mounted on microscopy glass slides in a 30 μL drop of Vectashield®. Excess mounting medium was removed with 3 MM paper and coverslips were directly sealed with clear nail polish.

Image acquisition, reconstruction and analysis for SIM

3D SIM imaging of fixed samples was carried out as described in Demmerle et al. (2017). SIM imaging was done using an ELYRA PS.1 super-resolution microscope system (ZEISS) equipped with 405,488,561 and 642 diode lasers and a 63x, 1.4 NA PlanApo oil immersion objective (immersion oil RI 1.512) and a pco.edge sCMOS camera (PCO). 3D SIM image stacks were acquired over the whole cell volume in z with 15 raw images (16 bit) per plane using five phases, three angles and 0.1 μm intervals. Raw data was computationally reconstructed using theoretical optical transfer functions (OTFs) and the ZEISS algorithm (ZEISS black, 2.3 SP1) yielding images with 130 nm lateral and 350 nm axial resolution. Color channels were aligned with parameters obtained from calibration measurements on 200 nm TetraSpeck beads (Invitrogen). All SIM data was routinely checked for quality and artifacts using SIMCheck (Ball et al., 2015).

Chromatin fractionation

Soluble and chromatin extracts were prepared as follows: cells were seeded in 10 cm-dishes, treated as indicated in the corresponding figure legends, washed three times with ice-cold PBS and harvested by trypsinization. The soluble fraction was extracted by incubation in ice-cold nuclear buffer (10 mM HEPES pH 7, 200 mM NaCl, 1 mM EDTA, 0.5% NP-40) supplemented with protease and phosphatase inhibitors (Roche) for 10 min on ice, and centrifuged at *2000 g* for 6 min. The remaining pellet was rinsed once with ice-cold washing buffer (10 mM HEPES pH 7, 50 mM NaCl, 0.3M sucrose, 0.5% Triton X-100) supplemented with protease and phosphatase inhibitors (Roche), which was removed by centrifugation at *1400 g* for 6 min. Finally, chromatin fractions were extracted by incubation in RIPA buffer (50 mM Tris-HCl pH 8, 150 mM NaCl, 1% IGEPAL CA-630, 0.1% SDS, 0.1% Na-deoxycholic acid) supplemented with protease and phosphatase inhibitors (Roche) and Benzonase® Nuclease (Sigma-Aldrich) for 30 min on ice and clarified by centrifugation at *max.* speed.

Immunoblotting

Whole cell extracts (WCE) were obtained by lysis in RIPA buffer (50 mM Tris-HCL pH 8.0, 150 mM NaCl, 1.0% IGEPAL CA-630, 0.1% SDS, and 0.1% Na-deoxycholic acid) supplemented with protease and phosphatase inhibitors (Roche) and Benzonase® Nuclease (Sigma-Aldrich) for 30 min. WCE, soluble and chromatin fractions were analyzed by SDS–PAGE after boiling samples in reducing buffer (DTT; Sigma-Aldrich) as per standard procedures.

For immunoblotting, primary antibodies were incubated ON at 4°C in PBS-T (0.05% PBS-Tween20) containing 3% powder milk. Milk was replaced by BSA for phospho antibodies' detection. Secondary peroxidase-coupled antibodies were incubated in PBS-T containing 5% powder milk at RT for 1h. ECL-based chemiluminescence was detected using an Amersham Imager 600.

Primary antibodies were used at the indicated dilutions: beta-actin (1/1000; Santa Cruz), CDC45 (1/200, Santa Cruz), CHK1-S345P (1/500; Cell signaling), ETAA1 (1/4000; in house), GINS3 (1/1000, Bethyl), HIST3 (1/1000, Abcam), MCM3 (1/500; Santa Cruz), PCNA (1/500, Santa Cruz), PolA1 (1/500; Abcam), POLD1 (1/1000, Abcam), POLE1 (1/1000, Abcam), Prim1 (1/500; Cell signaling), RPA1 (1/1000; Abcam), RPA2 (1/500; Novus Biologicals), TopBP1 (1/1000; Bethyl Laboratories) and γH2AX (1/2000; Millipore).

Egg extract and chromatin binding

Xenopus interphase egg extracts and sperm nuclei were prepared as previously described (Sannino et al., 2017). In brief, the day before of eggs collection, female frogs were injected twice, with 250 U and 650 U of chorionic gonadotropin (Sigma-Aldrich) respectively. Eggs were collected in 100 mM NaCl buffer. The eggs were then de-jellied in 10 mM Tris pH 8, 110 mM NaCl and 5 mM DTT (Sigma-Aldrich) and rinsed three times in MMR buffer (5 mM K-HEPES pH 7.5, 100 mM NaCl, 0.5 mM KCl, 0.25 mM $MgSO_4$, 0.5 mM $CaCl_2$, 25 μM EDTA). After that, eggs were released into interphase by addition of 5 μM calcium ionophore (Sigma-Aldrich) for 5-6 min, washed three times with MMR and rinsed twice in ice cold S-buffer (50 mM K-HEPES pH 7.5, 50 mM KCl, 2.5 mM $MgCl_2$, 250 mM sucrose, 15 μg/mL leupeptin, 2 mM β-mercaptoethanol (Sigma-Aldrich)). Activated eggs were then packed by centrifugation at *1200rpm* for 1 min and the excess of buffer was discarded. Eggs were crushed at *13000rpm* for 12 min at 4°C. The crude extract was collected and centrifuged at *70000rpm* for 12 min at 4°C in a TLA100 rotor (Beckman). The interphase extract was obtained by collecting and mixing the cleared cytoplasmic fraction together with the nuclear membranes.

For sperm nuclei preparation, testes were removed from male frogs that were injected the day before with 300 U of chorionic gonadotropin (Sigma-Aldrich), and they were placed in Petri dishes containing 10 mL EB buffer (50 mM KCl, 50 mM HEPES KOH pH 7.6, 5 mM $MgCl_2$, 2 mM DTT (Sigma-Aldrich)). Testis were then chopped with a razor blade and the material was transferred to 15 mL Falcon tubes. After that, the suspension was centrifuged at *2000 g* in a swinging bucket rotor for 5 min at 4°C. The pellet was resuspended in a total volume of 2 mL of RT SuNaSp buffer (0.25 M sucrose, 75 mM NaCl, 0.5 mM spermidine (Sigma-Aldrich), 0.15 mM spermine (Sigma-Aldrich)). To remove membranes, 100 μL of 2 mg/ml lysolecithin (Sigma-Aldrich) were added and incubated for 10 min at RT. Reaction was stopped by adding 3% BSA (Sigma-Aldrich). The pellet was resuspended again in 2 mL EB and spun at *2000 g* for 5 min at 4°C. The final pellet was resuspended in 400 μL of EB + 30% glycerol.

For chromatin binding, for each sample, sperm nuclei (4000 n/μL) were incubated at 23°C in 30 μL of egg extract. At the indicated times, reactions were stopped by diluting and mixing the extract with 300 μL EB (50 mM HEPES pH 7.4, 100 mM KCl, 2.5 mM $MgCl_2$) containing 0.25% NP-40, and centrifuged through a 0.5 M sucrose-EB layer at *10000 g* at 4°C for 5 min. Pellets were then washed once with EB and re-suspended in Laemmli buffer. Primary antibodies were used at the indicated dilutions: anti-*Xenopus* Orc1 (1:400000), anti-*Xenopus* Mcm7 (1:8000; Santa Cruz), anti-*Xenopus* RPA1 (1:40000), anti-*Xenopus* Pol 125 kDa (1:2000) and anti-CHK1-S345P (1:1000; Cell signaling).

Electron microscopy (EM)

DNA for electron microscopy analysis was processed as previously described with a few modifications (Hashimoto et al., 2010). Shortly, sperm nuclei (4000 n/μl) were incubated at 23°C in 200 μL egg extract for 60 min, diluted with 400 μL of EB buffer, layered onto 800 μL EB-EDTA (EB buffer + 1 mM EDTA) + 30% (w/v) sucrose and centrifuged at *3000 g* for 10 min at 4°C. Pellets were re-suspended in 100 μL EB-EDTA and transferred to a 96-well plate. 10 μg/ml of TMP (Sigma-Aldrich) were added to each well and samples were incubated for 5 min at 4°C in the dark and irradiated with 365 nm ultraviolet light for 7 min on a precooled metal block. This step was repeated 4 times. Samples were then supplemented with 0.1% (w/v) SDS to lysate nuclei and treated with 100 μg/ml RNase A (Thermo Fisher Scientific) for 1 h at 37°C. After that, psoralen-crosslinked chromatin was incubated with proteinase K (1 mg/ml; Sigma-Aldrich) for 2 h at 50°C. Finally, genomic DNA was extracted by adding one volume of 1:1 (v/v) phenol–chloroform mixture, precipitated with isopropanol, washed with 70% ethanol and processed for electron microscopy as previously shown in Hashimoto et al. (2010). Electron microscopy grid shadowing was done with a Leica MED20, and image acquisition with a FEI Tecnai 20 EM microscope equipped with a GATAN high-resolution camera at the IFOM electron microscopy facility. Blind analysis of EM images was performed by EM specialists.

Clonogenic and survival assays

For Clonogenic assay, cells were plated on 6-well plates (in triplicate) at a density of 300 cells/well. 24 h later, cells were treated with the indicated drug and concentration for 3 days. The colonies were grown for 7 additional days after which they were fixed and stained with 20% ethanol/0.1% crystal violet. Cells were then rinsed in water and colonies were counted manually.

To analyze cell survival, the number of U2OS/H2B-EGFP cells transfected and treated as indicated was daily analyzed by QIBC based on the GFP signal. Cells were seeded in triplicate.

QUANTIFICATION AND STATISTICAL ANALYSIS

Statistical details for each experiment can be found in the corresponding legend. Significance was assessed by Student's t test using GraphPad Prism 7.0. p = *, < 0.05; ****, < 0.0001.

DATA AND CODE AVAILABILITY

This study did not generate/analyze [datasets/code].